arXiv:cond-mat/0307520v1 [cond-mat.supr-con] 22 Jul 2003

Critical fluctuations and pseudogap observed in the microwave conductivity of BSCCO and YBCO thin films

D.-N. Peligrad*, and M. Mehring
2. Physikalisches Institut, Universität Stuttgart, 70550 Stuttgart, Germany

A. Dulčić
*Department of Physics, Faculty of Science, University of Zagreb, POB 331, 10002 Zagreb, Croatia**
(Dated: submitted: July 20, 2003; received on *condmat* December 23, 2021)

Critical fluctuations have been studied in the microwave conductivity of $Bi_2Sr_2CaCu_2O_{8+\delta}$, $Bi_2Sr_2Ca_2Cu_3O_{10+\delta}$, and $YBa_2Cu_3O_{7-\delta}$ thin films above T_c. It is found that a consistent analysis of the real and imaginary parts of the fluctuation conductivity can be achieved only if an appropriate wavevector or energy cutoff in the fluctuation spectrum is taken into account. In all of the three underdoped superconducting films one observes strong fluctuations extending far above T_c. The coherence length inferred from the imaginary part of the conductivity exhibits the static critical exponent $\nu = 1$ very close to T_c, and a crossover to the region with $\nu = 2/3$ at higher temperatures. In parallel, our analysis reveals the absence of the normal conductivity near T_c, i. e. fully opened pseudogap. Following the crossover to the region with $\nu = 2/3$, the normal conductivity is gradually recovered, i. e. the closing of the pseudogap is monitored.

PACS numbers: 74.40.+k, 74.25.Nf, 74.76.Bz

I. INTRODUCTION

Soon after the discovery of high-T_c superconductors it was found that fluctuations were more pronounced in these compounds than in the classical low temperature superconductors[1,2]. It is due primarily to short coherence lengths and large transition temperatures, but anisotropy and the degree of doping may also play a role. While classical low temperature superconductors exhibited only Gaussian type fluctuations,[3] it was estimated that high-T_c superconductors could give experimental access to a study of critical fluctuations[4]. Yet, early studies of the *dc* fluctuation conductivity[5,6] were interpreted within the Gaussian behavior, except for a narrow region (fraction of a degree) around T_c which was left out as possibly critical. Later on, the penetration depth measurements in $YBa_2Cu_3O_{7-\delta}$ revealed critical behavior as wide as $\pm$10K from T_c,[7] belonging to the universality class 3D XY. More recent measurements of thermal expansivity[8,9] and two-coil inductive measurements[10] have confirmed this wide range of critical fluctuations, while *dc* fluctuatuation conductivity measurements still claimed very narrow critical regions[11,12,13,14,15,16]. A major problem in the analysis of a *dc* fluctuation conductivity is to account for the short wavelength cutoff,[5,6,11,15] and energy cutoff[17,18] at higher temperatures. These effects are so strong that other inherent properties of the fluctuation conductivity can be obscured.

A more stringent test of a given theoretical model can be made through a study of the microwave fluctuation conductivity since it yields two experimental curves, one for the real part $\sigma_1(T)$, and the other for the imaginary part $\sigma_2(T)$, with different shapes but ensuing from the same physics assumed in the model. Some of the earlier microwave studies reported Gaussian and critical behavior,[19,20,21,22] but failed to account for the cutoff effects. However, a recent analysis has shown that the short wavelength cutoff yields a strong effect at higher temperatures, and a small, but experimentally detectable feature at T_c[23]. The latter was shown to be useful in setting a constraint on the cutoff parameters, which are then used in the whole temperature region above T_c. Further advantage of the *ac* fluctuation conductivity is that the imaginary part $\sigma_2(T)$ has no contribution from the normal electrons so that its analysis is free from subtraction problems often encountered in *dc* conductivity studies.

In this paper we present an analysis of the microwave fluctuation conductivity in $Bi_2Sr_2CaCu_2O_{8+\delta}$ (BSCCO-2212), $Bi_2Sr_2Ca_2Cu_3O_{10+\delta}$ (BSCCO-2223), and $YBa_2Cu_3O_{7-\delta}$ (YBCO) thin films. The central result is the temperature dependence of the coherence length which shows multiple critical regimes in each of the superconductors. Also shown in the present analysis is the reduction of the contribution of the normal conductivity in the measured real part $\sigma_1(T)$ of the complex conductivity. It is a direct evidence of the reduction of the one-electron density of states at the Fermi level, known as the pseudogap effect[24].

II. THEORETICAL BACKGROUND

In this paper, we use the expressions for the *ac* fluctuation conductivity which have been derived and extensively discussed recently[23]. The derivation was based on the time dependent Ginzburg-Landau theory and the approach introduced by Schmidt[25] long time ago. The new feature was the cutoff in the integration over the **k**-space which was imposed in order to comply with the slow variation principle of the Ginzburg-Landau theory[26]. Equivalent expressions were also obtained[27] from the linear response to an applied *ac* field[28].

In order to treat also the critical state, we have adopted the requirement that close to the superconducting transition all physical quantities should be expressed through the coherence length $\xi(T)$. In particular, the relaxation time of the lowest fluctuation mode becomes $\tau_0 \propto \xi^z$, where z is the dynamical critical exponent[29]. This is essential since the temperature dependence of the coherence length in the critical state takes a form different from that of the Gaussian or mean field result. On the other hand, the very form of the expressions obtained using the time dependent Ginzburg-Landau theory remain valid even in the critical state[30].

For the three dimensional (*3D*) anisotropic case the *ac* fluctuation conductivity is given by[23]

$$\widetilde{\sigma}^{\,3D} = \frac{e^2}{32\hbar\xi_{0c}} \left(\frac{\xi(T)}{\xi_0}\right)^{z-1} \int_0^{Q_{ab}} \int_{-Q_c}^{Q_c} \frac{4\, q_{ab}^3 \left[1 - i\Omega(1+q_{ab}^2+q_c^2)^{-1}\right]}{\pi(1+q_{ab}^2+q_c^2)[\Omega^2 + (1+q_{ab}^2+q_c^2)^2]}\, dq_{ab}\, dq_c \ , \tag{1}$$

where the prefactor is the well known Aslamazov-Larkin term,[26] except that the Gaussian temperature dependence $1/\sqrt{\epsilon}$ is replaced by that of the reduced coherence length $\xi(T)/\xi_0$. This dimensionless temperature dependent function is equal for both, the in-plane and c-axis coherence lengths, i. e. $(\xi_{ab}(T)/\xi_{0ab}) = (\xi_c(T)/\xi_{0c})$,[23] so that we omit the subscripts. The dimensionless parameter

$$\Omega(\omega, T) = \frac{\omega\tau_0}{2} = \frac{\pi}{16}\frac{\hbar\omega}{k_B T}\left(\frac{\xi(T)}{\xi_0}\right)^z \ , \tag{2}$$

involves the operating microwave frequency ω and the temperature dependence of the reduced coherence length. Note that we have used here the thermodynamically correct form $k_B T$, rather than the approximative $k_B T_c$ used before[23]. The latter will be used below only in theoretical simulations where $\xi(T)/\xi_0$ is used as the only variable. The cutoff in the fluctuation wavevector is introduced in $Q_{ab}(T) = k_{ab}^{max}\xi_{ab}(T) = \sqrt{2}\Lambda_{ab}\,\xi_{ab}(T)/\xi_{0ab}$ for the *ab*-plane and $Q_c(T) = k_c^{max}\xi_c(T) = \Lambda_c\,\xi_c(T)/\xi_{0c}$ along the *c*-axis, rather than a single cutoff on the modulus[27]. The analytical result of the integration in Eq. (1) and its application in the data analysis has been reported in detail[23]. A careful analysis has shown that, due to this cutoff, the real and imaginary parts of the *ac* fluctuation conductivity are not equal at T_c. The ratio $\sigma_2(T_c)/\sigma_1(T_c)$, which can be determined straightforwardly from the experimental data, puts a constraint on the choice of the parameters Λ_{ab} and Λ_c[23].

Time dependent Ginzburg-Landau approach is based on relaxational dynamics so that the dynamic critical exponent should be $z = 2$[31]. Indeed, it has been shown by expansion of the $\mathcal{S}$-functions in the limit of T_c that only for $z = 2$ one obtains a finite nonzero *ac* fluctuation conductivity, in agreement with experimental observations[23]. This value of the dynamic critical exponent was also found in Monte Carlo simulations for a vortex loop model of the superconducting transition[32].

With the slow variation principle alone, the parameters Λ_{ab} and Λ_c may be kept as constants from T_c up to any higher temperature. However, it has been shown recently that energy cutoff should also be imposed in order to satisfy the uncertainty principle for the minimum wave packet of the Cooper pairs[17,18]. For the anisotropic *3D* case one should have the condition

$$(\xi_0/\xi(T))^2 + 2\Lambda_{ab}^2 + \Lambda_c^2 = C\,, \tag{3}$$

where C is the energy cutoff parameter. At T_c the first term on the left hand side of Eq. (3) vanishes and one retrieves the pure wavevector cutoff condition. With the constraint ensuing from the experimental ratio $\sigma_2(T_c)/\sigma_1(T_c)$,[23] and Eq. (3) with a given energy cutoff parameter C, one can determine the Λ's at T_c. Within the concept of the energy cutoff, one should keep C fixed at all temperatures. Eq. (3) can then be satisfied only if the parameters Λ_{ab} and Λ_c become temperature dependent. It is reasonable to assume that their ratio $K = \Lambda_{ab}/\Lambda_c$ remains constant, i. e. as determined at T_c. Then, Eq. (3) yields both Λ's as functions of the reduced coherence length $\xi(T)/\xi_0$. With these replacements in our expressions for the *ac* fluctuation conductivity[23] one accounts also for the energy cutoff. One may remark that the value $C = 1$ implies that the minimum $\xi(T)$ is equal to ξ_0. However, for $C < 1$ the minimum $\xi(T)$ is bigger than ξ_0. This is important in high-T_c superconductors where ξ_0 is found to be unphysically small[23] so that the minimum $\xi(T)$ must be bigger than that value. It is given by $\min(\xi(T)) = \xi_0/\sqrt{C}$.

In order to illustrate the importance of the cutoff effects in a data analysis, we may simulate some cases. In Fig. 1 we present the calculated σ's for an isotropic superconductor. In that case, there is only one cutoff parameter Λ[23].

We have assumed that $(\sigma_2(T_c)/\sigma_1(T_c)) = 1.2$, which is a typical experimental value. It yields unequivocally the values $\Lambda = 0.1$, and $C = 0.03$. The σ's in Fig. 1 are calculated as functions of $(\xi_0/\xi(T))$ in order to make the presentation independent of the specific temperature dependence of the coherence length. The dotted, dashed and full lines in Fig. 1 present the calculated σ's using no cutoff, wavevector cutoff with the value of Λ fixed, and energy cutoff with C fixed, respectively. The upper three and lower three curves refer to σ_1 and σ_2, respectively. One can see that the cutoff brings about significant changes in the calculated curves so that great care is needed in attempts to fit a given set of experimental data.

If one assumes that the superconductor is anisotropic, one has to deal with two cutoff parameters. Assuming the same value for the ratio $(\sigma_2(T_c)/\sigma_1(T_c)) = 1.2$ as in Fig. 1, one can have the choices of the parameters Λ_{ab} and Λ_c as shown in Fig. 2[23]. An alternative presentation is possible in terms of the ratio $K = \Lambda_{ab}/\Lambda_c$ and the energy cutoff parameter C as shown in the inset to Fig. 2. The lower branch of this curve corresponds to the cases $\Lambda_{ab} \ll \Lambda_c$ while the upper branch is for $\Lambda_{ab} \gg \Lambda_c$. The crossover $\Lambda_{ab} = \Lambda_c$ is shown by the dotted line in the main panel of Fig. 2, and corresponds to $K = 1$ in the inset. In Fig. 3(a)-(c) we present the calculated σ's for three largely different choices of the cutoff parameters. The style of the presentation follows that of Fig. 1. We have argued earlier[23] that only the case with $\Lambda_{ab} \gg \Lambda_c$ is physically acceptable in anisotropic superconductors where $\xi_{0ab} \gg \xi_{0c}$. Here we present in Fig. 3(a) the results for energy cutoff and compare them to those for wavevector cutoff. The curves calculated with no cutoff are always added for the sake of reference. One can observe that both, σ_1 and σ_2 have well pronounced slopes at higher temperatures. The effect of the cutoff is to change those slopes. The effect of the energy cutoff is observable only at very high temperatures where the fluctuation conductivity rapidly vanishes. The choice $\Lambda_{ab} \ll \Lambda_c$ for the wavevector cutoff, and the accompanying choice $K \ll 1$ and $C = 1$ for the energy cutoff, are shown in Fig. 3(b). The shape of these curves are quite different from those of the previous case, thus showing the sensitivity of the numerical calculations to the choices of the cutoff parameters. Fortunately, the freedom of taking a diversity of choices for the cutoff parameters is restricted by physical arguments which make a large Λ_c unacceptable in systems having very small ξ_{0c}, as is the case in high-T_c superconductors[23]. Detailed analysis of the experimental data presented below, provide further support of this rule. Finally, we present also in Fig. 3(c) the case $\Lambda_{ab} = \Lambda_c$ which appears to be very similar, but not identical, to that of the isotropic case. It will also be shown as inadequate for the experimental data analysis shown later in this paper.

It is of interest for the data analysis in this paper to examine also the cutoff effects in two dimensional (*2D*) cases. The *ac* fluctuation conductivity is then given by[23]

$$\widetilde{\sigma}^{\,2D} = \frac{e^2}{16\hbar s}\left(\frac{\xi(T)}{\xi_0}\right)^z \int_0^Q \frac{4\,q^3\,\left[1 - i\Omega(1+q^2)^{-1}\right]}{(1+q^2)[\Omega^2 + (1+q^2)^2]}\,dq \ , \tag{4}$$

where s is the effective layer thickness. The wavevector cutoff is made only in the *ab*-plane with $k_{ab}^{max} = \sqrt{2}\Lambda/\xi_{0ab}$ while along the c-axis only the lowest $k_c = 0$ term is taken. Eq. (3) can again be applied for the energy cutoff. The calculated curves for σ_1^{2D} and σ_2^{2D} are shown in Fig. 4. We have used the *2D* cutoff parameter $\Lambda = 0.7$, i. e. equal to the choice of Λ_{ab} in the *3D* case of Fig. 3(a). In contrast to the *3D* case, we observe that the cutoff does not bring about a change in the slopes of σ_1^{2D} and σ_2^{2D} at higher temperatures.

The slopes of the σ's at higher temperatures are believed to be essential in an effort to determine the dimensionality of the fluctuations in an experimental analysis. Indeed, the slopes of the curves calculated with no cutoff in the *3D* and *2D* cases are different. However, the cutoff increases the slopes in the *3D* case as shown in Fig. 3(a). A direct comparison of the *2D* and *3D* curves in Fig. 5 shows that the cutoff makes the distinction between the two cases more difficult. The parameters ξ_{0c} and s in the prefactors of Eq. (1) and Eq. (4) determine just the offsets in the logarithmic plot of Fig. 5. These have been chosen so as to match the values of *2D* and *3D* calculations at higher temperatures. At temperatures closer to T_c it is easy to determine the dimensionality of the fluctuations, but at higher temperatures the two cases become indistinguishable.

It is worth noting that the above feature is pertinent not only to the *ac* but also to the *dc* fluctuation conductivity. Fig. 6 demonstrates that the cutoff affects strongly σ_{dc}^{3D} beyond some temperature, so that it becomes indistinguishable from that of σ_{dc}^{2D}. Hence, the dimensionality of the fluctuations cannot be infered from the behavior of the *dc* fluctuation conductivity at higher temperatures, provided that the cutoff effects are properly accounted for.

We may also remark that if only the wavevector cutoff were considered, the curves in Fig. 6 would acquire slope -6 in the limit of very high temperatures. If the coherence length acquired the Gaussian form $(\xi(T)/\xi_0) = 1/\sqrt{\epsilon}$ at those temperatures, the *dc* fluctuation conductivity would have the behavior $\sigma_{dc} \propto 1/\epsilon^3$ in both, *2D* and *3D* cases[11,15,27]. However, significant deviations from this behavior have been observed experimentally, and ascribed to the energy cutoff[17,18].

Finally, it may be of interest to compare the behavior of the *dc* fluctuation conductivity and the real part of the fluctuation conductivity in the *ac* case. Fig. 7 shows the corresponding *3D* curves calculated with the same set of parameters. Obviously, the fluctuation conductivity in the *dc* case diverges when T_c is approached, while σ_1 of the

ac case reaches a finite value. However, at higher temperatures, the information gained from a *dc* measurement is equivalent to that of the real part σ_1 in the *ac* case[23]. The imaginary part σ_2 is an additional information provided by an *ac* measurement.

Note that here we have considered only the fluctuation conductivity, but, for the sake of simplicity, no subscript has been used . The total conductivity above T_c includes also a contribution from the normal electrons. The latter has to be added to both, σ_{dc} and the real part σ_1 of the *ac* fluctuation conductivity, but not to the imaginary part σ_2 which is due solely to the superconducting electrons.

III. EXPERIMENTAL

We have measured a number of YBCO and BSCCO thin films grown on various substrates. The main features in our results did not change with the change of the substrate or thickness of the film. Here we report specifically on the measurements in an YBCO thin film (thickness 200 nm) grown on MgO substrate, BSCCO-2212 (350 nm) on $LaAlO_3$ and BSCCO-2223 (100 nm) on $NdGaO_3$. The sample was cut typically to 4 mm in length and 1 mm in width and mounted on a sapphire sample holder which extends to the center of an elliptical copper cavity resonating in ${}_{\rm e}{\rm TE}_{111}$ mode at ≈ 9.5 GHz. The sample was oriented with its longest side along the microwave electric field E_ω. In this configuration the microwave current flows only in the *ab*-plane of the film. The sapphire sample holder was thermally connected to a heater and sensor assembly but isolated from the body of the microwave cavity. With a temperature controller the temperature of the sample could be varied from 2 K up to room temperature. However, the cavity was kept in pumped helium flow at 1.7 K in order to eliminate spurious signals from cavity heating.

The measured quantity is the complex frequency shift $\Delta\widetilde{\omega}/\omega = \Delta f/f + i\,\Delta(1/2Q)$ in which the resonant frequency f and the Q-factor of the cavity change with the sample temperature. The empty cavity had $1/2Q$ close to 20 ppm, which was subtracted from the data measured with the sample. The level of $1/2Q$ with the sample in the normal state could be several hundred parts per million (ppm) and we were interested in detecting small changes due to the superconducting fluctuations above T_c. For this purpose it was beneficial to use the recently introduced modulation technique,[33] which enables the resolution of $\Delta(1/2Q)$ to 0.02 ppm. The resonant frequency of the cavity was measured by a microwave frequency counter.

For the film in the microwave electric field the cavity perturbation analysis yields[34]

$$\frac{\Delta\widetilde{\omega}}{\omega} = \frac{\Gamma}{N}\left[1 - N + \frac{(\widetilde{k}/k_0)^2 N}{\left[\coth(i\widetilde{k}d/2) + \tanh(i\widetilde{k}\zeta)\right] i\widetilde{k}d/2}\right]^{-1}, \tag{5}$$

where Γ is the filling factor of the sample in the cavity, and N is the depolarization factor of the film. The intrinsic property of the sample is its complex conductivity $\widetilde{\sigma} = \sigma_1 - i\sigma_2$. It is contained in the complex wavevector $\widetilde{k} = k_0\sqrt{1 - i\widetilde{\sigma}/(\epsilon_0\omega)}$, where $k_0 = \omega\sqrt{\mu_0\epsilon_0}$ is the vacuum wavevector. The thickness of the film is d, and ζ is the asymmetry parameter due to the substrate.[34] The unknown parameters in Eq. (5) can be evaluated from the ratio of the slopes of the experimental curves $\Delta(1/2Q)$ and $\Delta f/f$ in the normal state far above T_c, provided that the normal state conductivity is known at the temperature where the experimental slopes were evaluated. Eq. (5) can then be used to convert the experimental data for $\Delta(1/2Q)$ and $\Delta f/f$ at any temperature to obtain the corresponding experimental values of σ_1 and σ_2.

IV. BSCCO-2212

Fig. 8 shows the experimental data of BSCCO-2212 thin film and the complex conductivity deduced from these data by means of Eq. (5). One can observe clearly the peak in the real part (σ_1) due to the superconducting fluctuations. Its maximum appears when the coherence length diverges,[28,29] and this occurs at the critical temperature of the superconducting transition. The imaginary part (σ_2) rises from its zero value found above T_c, to a saturation at low temperatures.

The total experimentally determined conductivity above T_c may include the contributions due to the normal conductivity and the superconducting fluctuation conductivity. In all previously reported *dc* conductivity measurements, it was assumed that the experimentally observed conductivity was the sum $\sigma^{exp} = \sigma_n + \sigma$. The normal conductivity near T_c was obtained from the extrapolated linear resistivity far above T_c. Hence, the fluctuation conductivity σ was obtained upon subtraction $\sigma^{exp} - \sigma_n$, and then analyzed. This approach, however, neglects the effect of the pseudogap which has been observed by other techniques in high-T_c superconductors[24]. The opening of the pseudogap reduces the density of one electron states at the Fermi level so that the normal conductivity is also reduced below σ_n. The

pseudogap is observed in optimally doped samples near T_c, and in underdoped samples even well above T_c. If the pseudogap is fully opened near T_c, the normal conductivity should completely vanish, and the whole experimentally observed conductivity should be due to the fluctuation conductivity, i. e. $\sigma^{exp} = \sigma$.

We have analyzed our measured microwave conductivity, with and without subtracting the extrapolated σ_n from the real part σ_1^{exp}. Fig. 9(a) shows on an enlarged scale around T_c the two sets of data, i. e. σ_1^{exp}, and $\sigma_1^{exp} - \sigma_n$. The inset in Fig. 9(a) shows a linear ρ_n fitted to the real part of the resistivity at temperatures above 150 K. This linear ρ_n is shown extrapolated to lower temperatures. It is used to calculate the extrapolated normal conductivity $\sigma_n = 1/\rho_n$ shown by the dotted line in the main panel of Fig. 9(a). Note that the imaginary part σ_2 is due solely to the superconducting fluctuations, i. e. σ_2 is background free so that no subtraction should be in place. It is obvious that the experimental ratio σ_2/σ_1 at T_c is different in the two sets of data. This ratio is important in the determination of the cutoff parameters as discussed in Section II. In this paper, we study the conductivities above T_c shown in Fig. 9(b) as functions of the reduced temperature $\epsilon = \ln(T/T_c)$.

We shall first consider the conventional approach in which σ_n is subtracted. In that case we find σ_2/σ_1=1.46 at T_c, and use this value to set a constraint on the choices of the cutoff parameters.[23] The inset in Fig. 10(a) shows the relationship between the parameters $K = \Lambda_{ab}/\Lambda_c$ at T_c and the energy cutoff parameter C defined in Eq. (3). Taken an allowed choice of the cutoff parameters, one can equate the imaginary part of Eq. (1) to the experimental value of σ_2, and solve numerically for the reduced coherence length $\xi(T)/\xi_0$. Note that the parameter ξ_{0c} in the prefactor of Eq. (1) can be determined straightforwardly from the value of σ_2 at T_c where $\xi(T)/\xi_0$ diverges. Namely, the value of σ_2 at T_c is practically insensitive to the choice of the cutoff parameters which can, for that purpose, be set to any value[23]. Here we obtained $\xi_{0c} = 0.05$ nm. Once the values of the reduced coherence length $\xi(T)/\xi_0$ are calculated for all the experimental points, one can use them in the real part of Eq. (1) to calculate σ_1 and compare with the experimental data. Fig. 10 shows the results for several choices of the cutoff parameters. The concomitant coherence lengths are presented in Fig. 11. Near T_c one obtains the same values for the coherence length regardless of the choice of the cutoff parameters. This is due to the fact that σ_2 is practically insensitive to the wavevector cutoff in that temperature region. It appears that very close to T_c the coherence length follows the critical exponent $\nu = 1$. The differences between the various choices appear at higher temperatures.

Let us first look at the anisotropic *3D* case with $C = 1$ and $K \gg 1$. It yields the coherence length in Fig. 11 having the critical exponent $\nu = 2/3$ pertaining to the $3D$ XY universality class. This behavior would be in agreement with the results of other experiments [8,9,10]. However, the calculated σ_1 fits the experimental data only near T_c as seen in Fig. 10. At higher temperatures the calculated σ_1 overestimates the experimental fluctuation conductivity represented by the data set $\sigma_1 = \sigma_1^{exp} - \sigma_n$. This overestimation has no physical explanation. Therefore, we should reject this choice of the cutoff parameters.

The choice $K = 1$ entails the condition $C \ll 1$ so that the energy cutoff is more severe. The calculated σ_1 is therefore more reduced at higher temperatures, and the overall fit to the experimental points appears to be improved (cf. Fig. 10). However, some overestimation is still present, in particular at high temperatures, so that this solution should also be rejected. Even stronger argument for the rejection comes from the inspection of the concomitant coherence length in Fig. 11. At higher temperatures, its slope is reduced well below the value 2/3 found in other experiments. This is particularly well seen in Fig. 11(b) where high temperature region is presented on an enlarged scale. The reduced slope appears as the mathematical result of the strong energy cutoff $C \ll 1$.

For $K \ll 1$ the calculated σ_1 overestimates largely the experimental values at higher temperatures. Hence, this choice of the cutoff parameters can be rejected, too.

We may also look at the results of the *2D* calculation based on the expression given in Eq. (4). One can adjust the parameters so that the calculated σ_1 fits the experimental data very well at higher temperatures as seen in Fig. 10. Therefore, one might be tempted to consider the scenario in which the system obeys the anisotropic *3D* behavior with $K \gg 1$ and $C = 1$ at temperatures close to T_c followed by a crossover to a *2D* behavior at higher temperatures. This scenario could yield an overall good fit to the experimental data, except at very high temperatures (cf. Fig. 10(b)). However, the coherence length obtained in the *2D* calculation is physically unacceptable because of the saturation at high temperatures as seen in Fig. 11. Having explored all the possibilities, we have to conclude that none of the above scenarios yields a satisfactory result with the data set $\sigma_1 = \sigma_1^{exp} - \sigma_n$.

Next, we turn to the case in which no subtraction is made so that the whole experimental σ_1^{exp} near T_c is attributed to the fluctuation conductivity σ_1. From Fig. 9 we find first $\sigma_2/\sigma_1 = 1.22$ at T_c, and find the corresponding curve for the cutoff parameters in the inset of Fig. 12(a). It is quite different from that of the preceding case in the inset of Fig. 10(a). The data analysis can be done as before and the results for the various choices of the cutoff parameters are shown in Fig. 12, while the concomitant coherence lengths are presented in Fig. 13.

The highest temperature where σ_2 is still detectable beyond the noise level is $\epsilon = 0.5$ (145 K). At that temperature, σ_2 has decreased by four orders of magnitude from its value at T_c (Fig. 12(b)), and further on our signal is lost in the experimental noise. Our method of analysis relies on the experimental values of σ_2 to calculate the reduced coherence length. Hence, the latter is also available only up to this same temperature (Fig. 13). The same applies to σ_1 which is

calculated from the coherence length. Beyond this temperature, the measured conductivity contains only the nonzero real part σ_1^{exp}, which is shown in Fig. 12 up to $\epsilon = 0.66$ (170 K).

One observes in Fig. 12 that the anisotropic *3D* expressions with $K = 2.5$ and $C = 0.065$ yield σ_1 which matches very well the experimental data up to $\epsilon \approx 0.1$. At higher temperatures the calculated values deviate from the experimental points, but in this case the deviation falls below the data and can be physically explained. Namely, the calculated σ_1 is the fluctuation contribution. At temperatures close to T_c there is no normal conductivity contribution if the pseudogap is fully opened so that the calculated fluctuation conductivity σ_1 equals the measured σ_1^{exp}. Beyond some temperature, the pseudogap starts to close and the normal conductivity contribution appears gradually growing from zero to its full value σ_n at high temperatures. This growing normal conductivity contribution is seen in Fig. 12 as the difference between the experimental points and the calculated fluctuation conductivity σ_1 shown by the full line. A more detailed discussion of the pseudogap will be given in a subsequent section.

The other choices of the cutoff parameters used in the *3D* calculations are also presented in Fig. 12. The fits of the calculated σ_1 to the experimental data are less good. Also, the coherence length does not follow the expected slope 2/3 in Fig. 13.

The *2D* analysis is particularly interesting. One can choose the parameters so that the calculated σ_1 is practically indistinguishable from that of the best anisotropic *3D* choice in Fig. 12. Also, the coherence length obtained in the *2D* calculation approaches the slope 2/3 at higher temperatures. The indistinguishability of the *3D* and *2D* behavior at higher temperatures has already been discussed in Section II. Here we may examine whether a *3D* to *2D* crossover is a possible scenario. A crude criterion for the crossover is that $\xi_c(\epsilon)$ becomes comparable to $s/2$. The *2D* curves in Fig. 12 were calculated with $s = 3$ nm so that the above criterion is met when $\xi_c(\epsilon^*) \approx 1.5$ nm. Since $\xi_{0c} = 0.05$ nm is determined from Eq. (1) and the experimental value of σ_2 at T_c, one finds $\xi_c(\epsilon^*)/\xi_{0c} \approx 30$. From Fig. 13 one finds that this condition corresponds to $\epsilon^* \approx 0.06$. This value is in accord with the observation of a good fit of the calculated σ_1^{2D} to the experimental data in Fig. 12. From that point of view, the *3D-2D* crossover appears as a likely scenario. However, the coherence length in the *2D* case does not reach the slope 2/3 at that temperature, but only at a much higher one ($\epsilon \approx 0.18$). Therefore, one does not find decisive arguments in favor of the *3D-2D* crossover in BSCCO-2212.

Having established the consistent analysis of the data, we may comment on the resulting coherence length. Fig. 12 reveals the existence of two critical regimes with the static critical exponents $\nu = 2/3$ well above T_c, and a crossover to $\nu = 1$ when T_c is approached. The former critical regime corresponds to the $3D$ XY universality class, and has been reported before [8,9,10]. However, the well defined crossover to the critical regime with $\nu = 1$ is novel and surprising. We may also remark that our analysis yields not only the slopes, but also the absolute values of the reduced coherence length. Thus, we observe that these absolute values are very high, much higher than those predicted by the mean field or Gaussian expression $(\xi(T)/\xi_0) = 1/\sqrt{\epsilon}$. Note also that the crossover between the two critical regimes is not just a change of the slopes but involves a step in the absolute values of the reduced coherence length. We find that the critical behaviour persists as far above T_c as the reduced coherence length is still large.

Also important is to comment on the smallness of the parameter $\xi_{0c} = 0.05$ nm found above. Such small values were also obtained in the analysis of the *dc* fluctuation conductivity[5]. It is to be noted that this parameter is not the zero temperature coherence length, but the coefficient in the linear term of the Ginzburg-Landau functional. The zero temperature coherence length should have a larger, physically acceptable dimension. Also, the obtained value for ξ_{0c} is certainly too small to represent the shortest length for the variation of the order parameter. In fact, the above analysis based on the energy cutoff yields $\min(\xi_c(T)) = \xi_{0c}/\sqrt{C}$. In the present case with $C = 0.065$ as in Fig. 13(a), one obtains $\min(\xi_c) = 0.2$ nm. This is large enough to be physically acceptable for the shortest variation of the coherence length along the c-axis.

The above calculations were all carried out with energy cutoff, but the main conclusions of the analysis remain valid even if only wavevector cutoff is taken. Fig. 14 shows a comparison of the calculations with wavevector and energy cutoffs. In the former approach, Λ_{ab} and Λ_c are determined at T_c by the experimental ratio $\sigma_2(T_c)/\sigma_1(T_c)$, and then kept fixed at all temperatures. On the contrary, in the energy cutoff approach, the values of Λ_{ab} and Λ_c are reduced at higher temperatures according to Eq. (3). Their temperature variation is shown in the inset of Fig. 14(a). One can readily observe that there is practically no difference between the two approaches over most of the temperature range covered by the actual data. Only at the highest temperatures one observes a slightly stronger decrease of the calculated values when the energy cutoff is applied.

V. BSCCO-2223

Fig. 15 shows the measured complex frequency shift and the conductivity in BSCCO-2223 thin film. The main features are similar to those observed in BSCCO-2212 thin film. The transition here appears to be broader and T_c is lower, both indicating that the sample is underdoped. We have carried out the complete analysis for each of the

various cases as described in the preceding section. Fig. 16 shows the conductivities with and without the subtraction of the extrapolated normal conductivity σ_n. The analysis based on the subtracted data set is shown in Fig. 17 and the concomitant coherence lengths are shown in Fig. 18. One can easily verify that none of the choices for the cutoff parameters can yield satisfactory results with this data set. This is parallel to the conclusion reached above in the case of BSCCO-2212.

If the unsubtracted data set with $\sigma_1 = \sigma_1^{exp}$ is taken, one gets the best fit using the anisotropic *3D* expression with $K = 3.9$ and $C = 0.08$ as shown in Fig. 19. The other choices for the cutoff parameters yield σ_1 curves which depart from the experimental points much earlier. Also important is to observe that the concomitant coherence length in Fig. 20 deviate from the slope 2/3.

As for the *2D* calculation, one observes that the coherence length acquires exactly the slope 2/3 at $\epsilon = 0.1$, and the calculated σ_1^{2D} is found on the data points in Fig. 19. The parameter $s = 1.2$nm was used in the *2D* calculations in this case. The *3D-2D* crossover is expected at $\xi_c(\epsilon^*) = s/2 = 0.6$nm. From $\sigma_2(T_c)$ one finds $\xi_{0c} = 0.016$ nm in BSCCO-2223 so that $\xi_c(\epsilon^*)/\xi_{0c} = 38$, and finally from Fig. 20 one can evaluate $\epsilon^* = 0.05$. Fig. 19(c) shows on an enlarged scale that the calculated σ_1^{2D} fits very well to the experimental points at that temperature. Hence, the *3D-2D* crossover is a likely scenario in BSCCO-2223.

An enlarged view of the coherence length at higher temperatures in Fig. 20(b) reveals that there is a step in the temperature dependence of the coherence length. The origin of this feature is not yet known. We may only speculate that it is due to the multiple layer structure of BSCCO-2223.

Also important is to notice in the behaviour of σ_1 in Fig. 19(a) that the normal conductivity starts to recover its full value at higher temperatures than in BSCCO-2212. It means that the pseudogap is fully opened up to a relatively higher temperature. This will be discussed in detail in a subsequent section.

VI. YBCO

The experimental complex frequency shift and microwave conductivity in YBCO thin film is shown in Fig. 21. The transition appears to be sharper than in BSCCO thin films. This already points that the fluctuations in YBCO are weaker. The conductivities are shown in Fig. 22 with the two data sets. One can observe that the ratio $\sigma_2(T_c)/\sigma_1(T_c)$ varies between the two sets much more than in the case of BSCCO samples. Also one observes that σ_2 drops much faster in YBCO. Already at $\epsilon = 0.2$ it has decreased by four orders of magnitude from its value at T_c, and then turns into noise around zero value. Therefore, the coherence length can only be calculated up to this temperature. The same holds for the calculation of σ_1 as shown in the various cases below.

The full analysis based on the data set with subtracted σ_n from σ_1^{exp} is presented in Fig. 23 and the concomitant coherence lengths are shown in Fig. 24. The *3D* case with $K \gg 1$ yields σ_1 values which overestimate the experimental points at higher temperatures so that one should reject this choice. The other choices of the cutoff parameters yield lower calculated σ_1 but the corresponding coherence lengths have slopes which deviate from the expected 2/3 value. Only the *2D* coherence length approaches the slope 2/3, but the fit of σ_1 in Fig. 23 is poor so that even this case has to be rejected.

The analysis of the data set where no subtraction was made is shown in Fig. 25 and the concomitant coherence lengths are presented in Fig. 26. The best choice of the *3D* cutoff parameters is $K = 4.7$ and $C = 0.08$. It yields the slope 2/3 for the coherence length at higher temperatures. The calculated σ_1^{3D} deviates early from the experimental points in Fig. 25. This means that the pseudogap starts to close very soon and the normal conductivity grows rapidly, reaching its full value already at $\epsilon = 0.2$. Regarding the dimensionality, we find that a *2D* calculation yields also the slope 2/3 for the coherence length at temperatures above $\epsilon \approx 0.04$. Since $s = 6.5$ nm was used in this *2D* calculation, one may expect the *3D-2D* crossover when $\xi_c(\epsilon^*) = s/2 = 3.8$ nm. From σ_2 at T_c in YBCO we found $\xi_{0c} = 0.07$ nm so that the crosover should occur at the reduced coherence length $\xi_c(\epsilon^*)/\xi_{0c} = 47$. Using the data in Fig. 26(a) one finds $\epsilon^* \approx 0.015$. The calculated σ_1^{2D} crosses the experimental points in Fig. 25(a) around this same temperature. Hence, the *3D-2D* crossover in YBCO is not excluded already at temperatures so close to T_c.

The coherence length (Fig. 26) shows again the two critical regimes as in the BSCCO samples, but their temperature range is squeezed closer to T_c. The $3D$ XY critical regime with $\nu = 2/3$ is found within $0.05 < \epsilon < 0.12$. This finding is in agreement with the combined analysis of the *dc* conductivity, specific heat, and susceptibility measurements in YBCO single crystals[35].

The point of interest is also to look at the absolute values of the reduced coherence length. Theese are much lower in YBCO than in BSCCO samples at the same temperature above T_c. The observation made above, that the absolute values of the reduced coherence length are essential for the critical behaviour, appears to be confirmed. In other words, a given critical regime persists as long as the reduced coherence length has high enough values. Due to the divergence of the coherence length in the limit of T_c, one always has to reach this condition. Thus, in classical low temperature superconductors, the critical regime should also occur, but only within a tiny temperature interval

around T_c which is experimentally unaccessible. In high-T_c superconductors, however, this temperature interval is very much extended. As the analysis in the present paper shows, there is a systematic extension of the critical regime towards higher temperatures in YBCO, BSCO-2212, and BSCCO-2223 samples.

VII. PSEUDOGAP

It has been shown in the preceding sections that in all our samples the consistent analysis of the data could be made when no subtraction of the normal conductivity was made near T_c. This feature is profoundly different from that known in conventional low temperature superconductors. Obviously, the fact that superconducting fluctuations are orders of magnitude stronger in layered high-T_c superconductors, makes their physical behaviour quite different. It has been observed using other experimental methods that one electron density of states at the Fermi surface start to diminish already well above T_c. This phenomenon has been named the pseudogap [24]. Our analysis of the microwave fluctuation conductivity has shown that the depletion of the normal electrons is dramatic near T_c. There, the system obeys the critical regime with $\nu = 1$ and a crossover to the $3D$ XY critical regime with $\nu = 2/3$. As the latter regime evolves further by reducing the coherence length, there appears gradually some normal conductivity which adds to the fluctuation conductivity to make the experimentally observed one. In Fig. 27 we present the growth of this normal conductivity to its full value σ_n in our samples. The presentation is made with the calculated fluctuation conductivity σ_1 in both, *3D* and *2D* cases. Only positive values for the reduced normal conductivity are physically acceptable. Hence, YBCO is seen to behave certainly as a *3D* system at temperatures very close to T_c. Ony at $\epsilon > 0.015$ the *2D* behavior becomes a possible scenario since the calculated normal conductivity becomes positive. In BSCCO-2212 the *3D* behavior is established up to $\epsilon \approx 0.06$. At higher temperatures the values of the normal conductivity calculated in the *2D* case become also positive, and not much different from the *3D* case. The interesting situation occurs with BSCCO-2223. There, the corresponding values calculated in the *3D* case vanish at temperatures from T_c up to $\epsilon \approx 0.05$, which is the sign of the fully opened pseudogap. In that temperature region, the *2D* calculation yields physically unacceptable negative values. In the interval $0.05 < \epsilon < 0.1$ the *3D* calculation yields negative values while the *2D* calculation now retains the zero values characteristic of the still fully opened pseudogap. Hence, we conclude that *3D-2D* crossover has taken place at $\epsilon^* \approx 0.05$. At $\epsilon > 0.1$, the *3D* calculation yields again positive values for the normal conductivity. At higher temperatures they become even indistinguishable from those of the *2D* case. However, a reversed crossover from *2D* to *3D* behavior at higher temperatures is physically unacceptable because the coherence length does not increase but continues to shrink to ever smaller values. Therefore we may conclude that the system remains *2D* at all temperatures above $\epsilon^* \approx 0.05$. In view of this observation, we may suggest that the formal indistinguishability of the *2D* and *3D* cases at higher temperatures should be interpreted in favor of the *2D* behavior.

It was shown by Corson et al. [36] that underdoped BSCCO-2212 had extended region of superconducting fluctuations above T_c. The evidence for superconducting fluctuations in underdoped high-T_c superconductors was found also from the measurement of the Nernst effect [37,38]. These results could support the interpretation of the pseudogap as preformed Cooper pairs above T_c [39]. However, direct relationship of the superconducting fluctuations to the pseudogap could not be made. The relevant study of the pseudogap features could be achieved by other experimental techniques [24]. The analysis given in the present paper shows that both, superconducting fluctuations and the pseudogap, can be studied by the same experimental technique. A single set of data can be used to establish a direct relationship of the superconducting fluctuations to the pseudogap in a given sample. We find that the two phenomena are indeed intimately related. Namely, the growing normal conductivity discussed above is the difference of the experimental values and the calculated fluctuation conductivity σ_1. The latter could be calculated due to the direct measurement of the imaginary part σ_2. One should note that the detection of σ_2 is a sign of the presence of the superconducting fluctuations. Due to the high sensitivity of our experimental setup, we could measure the decay of σ_2 over four orders of magnitude from T_c up to some sample dependent higher temperature. When this evolution is compared to that shown in Fig. 27, one finds that the intensity of the superconducting fluctuations is related to the opening of the pseudogap. In our YBCO sample, the superconducting fluctuations diminish relatively soon above T_c, and the normal conductivity recovers up to the full σ_n, i. e. the pseudagap closes. In more underdoped BSCCO-2223 sample, the critical fuctuations extend to much higher temperatures, and the pseudogap is seen to follow this behaviour concomitantly. We find this observation to be a strong argument that the loss of the one electron states at the Fermi level, which constitutes the main feature of the pseudogap, is due to the strong participation of the electrons in the superconducting fluctuations.

VIII. CONCLUSIONS

We have measured complex microwave conductivity in $Bi_2Sr_2CaCu_2O_{8+\delta}$, $Bi_2Sr_2Ca_2Cu_3O_{10+\delta}$, and $YBa_2Cu_3O_{7-\delta}$ thin films above T_c. We have found that the experimental curves for the real and imaginary part of the *ac* fluctuation conductivity can be consistently interpreted only if the theoretical expressions take into account a proper wavevector or energy cutoff in the fluctuation spectrum. Strong fluctuations extending far above T_c were observed in all of the three underdoped superconducting films. Our analysis yields the temperature dependence of the coherence length. Quite surprisingly, we observe multiple critical regions. Near T_c the static critical exponent appears to be $\nu = 1$. Following a crossover, one finds $\nu = 2/3$ at higher temperatures. This evolution is paralleled by closing of the pseudogap as seen directly in our analysis through the contribution of the normal conductivity in the total experimentally observed one.

Acknowledgments

D.-N. Peligrad and M. Mehring acknowledge support by the Deutsche Forschungsgemeinschaft (DFG) project Nr. Me362/14-2. A. Dulčić acknowledges support from the Croatian Ministry of Science. D. -N. Peligrad acknowledge also V. Rădulescu for the help in the development of some of the required software for data analysis.

---

* present address: Philips Research Laboratories, Weisshausstrasse 2, D-52066, Aachen, Germany
Electronic address: D.-N. Peligrad (dragos.peligrad@philips.com); M. Mehring (m.mehring@physik.uni-stuttgart.de); A. Dulčić (adulcic@phy.hr)

[1] P. P. Freitas, C. C.Tsuei, T. S. Plaskett, Phys. Rev. **B36**, 833 (1987).
[2] M. Ausloos and Ch. Laurent, Phys. Rev. **B37**, 611 (1988).
[3] W. J. Skocpol and M. Tinkham, Rep. Prog. Phys. **38**, 1049 (1975).
[4] C. J. Lobb, Phys. Rev. **B36**, 3930 (1987).
[5] R. Hopfengärtner, B. Hensel, and G. Saemann-Ischenko, Phys. Rev. **B44**, 741 (1991).
[6] A. Gauzzi and D. Pavuna, Phys. Rev. **B51**, 15420 (1995).
[7] S. Kamal, D. A. Bonn, N. Goldenfeld, P. J. Hirschfeld, R. Liang, and W. N. Hardy, Phys. Rev. Lett. **73**, 1845 (1994).
[8] V. Pasler, P. Schweiss, C. Meingast, B. Obst, H. Wühl, A. I. Rykov, and S. Tajima, Phys. Rev. Lett. **81**, 1094 (1998).
[9] C. Meingast, V. Pasler, P. Nagel, A. Rykov, S. Tajima, and P. Olsson, Phys. Rev. Lett. **86**, 1606 (2001).
[10] K. D. Osborn et al., cond. mat 0204417, unpublished.
[11] M. R. Cimberle, C. Ferdeghini, E. Giannini, D. Marré, M.Putti, A. Siri, F. Federici, and A. Varlamov, Phys. Rev. **B55**, R14745 (1997).
[12] R. Menegotto Costa, P. Pureur, L. Ghivelder, J. A. Campá, and I. Rasines, Phys. Rev. **B56**, 10836 (1997).
[13] S. H. Han, Yu. Eltsev, and Ö. Rapp, Phys. Rev. **B57**, 7510 (1998).
[14] S. H. Han, Yu. Eltsev, and Ö. Rapp, Phys. Rev. **B61**, 11776 (2000).
[15] E. Silva, S. Sarti, R. Fastampa, and M. Giura, Phys. Rev. **B64**, 144508 (2001).
[16] R. Menegotto Costa, P. Pureur, M. Gusmão, S. Senoussi, and K. Behnia, Phys. Rev. **B64**, 214513 (2001).
[17] C. Carballeira, S. R. Currás, J. Viña, J. A. Veira, M. V. Ramallo, and F. Vidal, Phys. Rev. **B63**, 144515 (2001).
[18] J. Viña, J. A. Campá, C. Carballeira, S. R. Currás, A. Maignan, M. V. Ramallo, I. Rasines, J. A. Veira, P. Wagner, and F. Vidal, Phys. Rev. **B65**, 212509 (2002).
[19] S. M. Anlage, J. Mao, J. C. Booth, D. H. Wu, and J. L. Peng, Phys. Rev. **B53**, 2792 (1996).
[20] J. C. Booth, D. H. Wu, S. B. Qadri, E. F. Skelton, M. S. Osofsky, A. Piqué, and S. M. Anlage, Phys. Rev. Lett **77**, 4438 (1996).
[21] G. Nakielski, D. Görlitz, Chr. Stodte, M. Welters, A. Krämer, and J.Kötzler, Phys. Rev. **B55**, 6077 (1997).
[22] J. R. Waldram, D. M. Broun, D. C. Morgan, R. Ormeno, and A. Porch, Phys. Rev. **B59**, 1528 (1999).
[23] D.-N. Peligrad, M. Mehring, and A. Dulčić, Phys. Rev. **B67**,174515 (2003).
[24] T. Timusk and B. Statt, Rep. Prog. Phys. **62**, 61 (1999).
[25] H. Schmidt, Z. Phys. **216**, 336 (1968).
[26] M. Tinkham, *Introduction to Superconductivity,* 2nd ed. (McGraw-Hill, New York, 1995).
[27] E. Silva, Eur. Phys. J. B **27**, 497 (2002).
[28] A. T. Dorsey, Phys. Rev. **B43**, 7575 (1991).
[29] D. S. Fisher, M. P. A. Fisher, and D. A. Huse, Phys. Rev. **B43**, 130 (1991).
[30] R. A. Wickham and A. T. Dorsey, Phys. Rev. **B61**, 6945 (2000).
[31] P. C. Hohenberg and B. I. Halperin, Rev. Mod. Phys. **49** 435 (1977).
[32] V. Aji and N. Goldenfeld, Phys. Rev. Lett. **87**, 197003 (2001).

[33] B. Nebendahl, D.-N. Peligrad, M. Požek, A. Dulčić, and M. Mehring, Rev. Sci. Instr. **72**, 1876 (2001).
[34] D.-N. Peligrad, B. Nebendahl, M. Mehring, A. Dulčić, M. Požek and D. Paar, Phys. Rev. B **64**, 224504 (2001).
[35] M. V. Ramallo and F. Vidal, Phys. Rev. **B59**, 4475 (1999).
[36] J. Corson, R. Mallozzi, J. Orenstein, J. N. Eckstein, and I. Bozovic, Nature **398**, 221 (1999).
[37] Z. A. Xu et al., Nature **406**, 486 (2000).
[38] Y. Wang et al., Phys. Rev. **B64**, 24519 (2001).
[39] V. J. Emery and S. A. Kivelson, Nature **374**, 434 (1995).

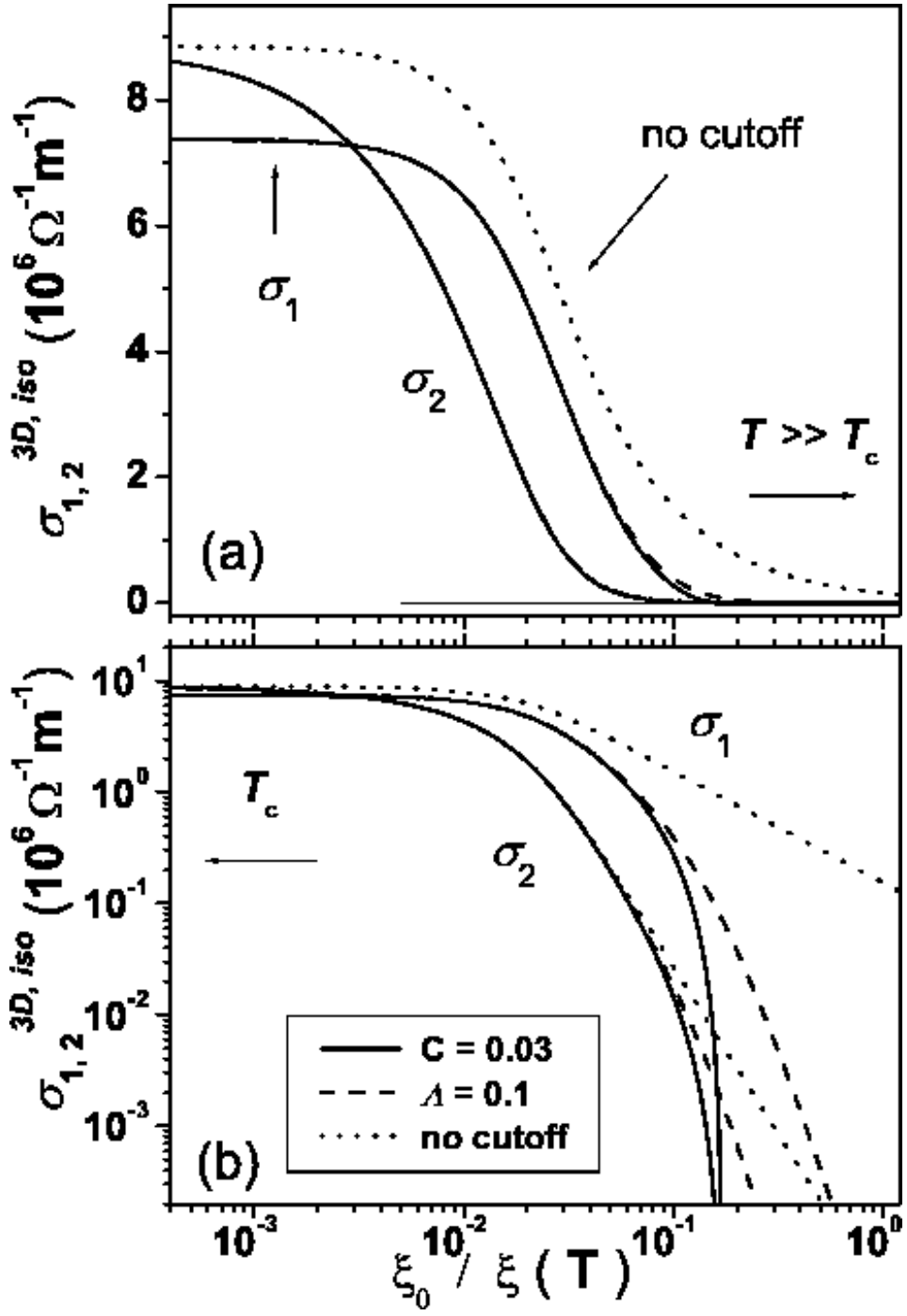


FIG. 1: Calculated *ac* fluctuation conductivity in the isotropic *3D* case. The dotted lines show the results in the case when no cutoff is taken into account. The dashed lines are obtained with the wavevector cutoff ($\Lambda = 0.1$) consistent with the ratio $(\sigma_2(T_c)/\sigma_1(T_c)) = 1.2$, which is a typical experimental value. The full lines involve the energy cutoff ($C = 0.03$) that matches the wavevector cutoff at temperatures close to T_c. The upper and lower curves represent σ_1 and σ_2, respectively.

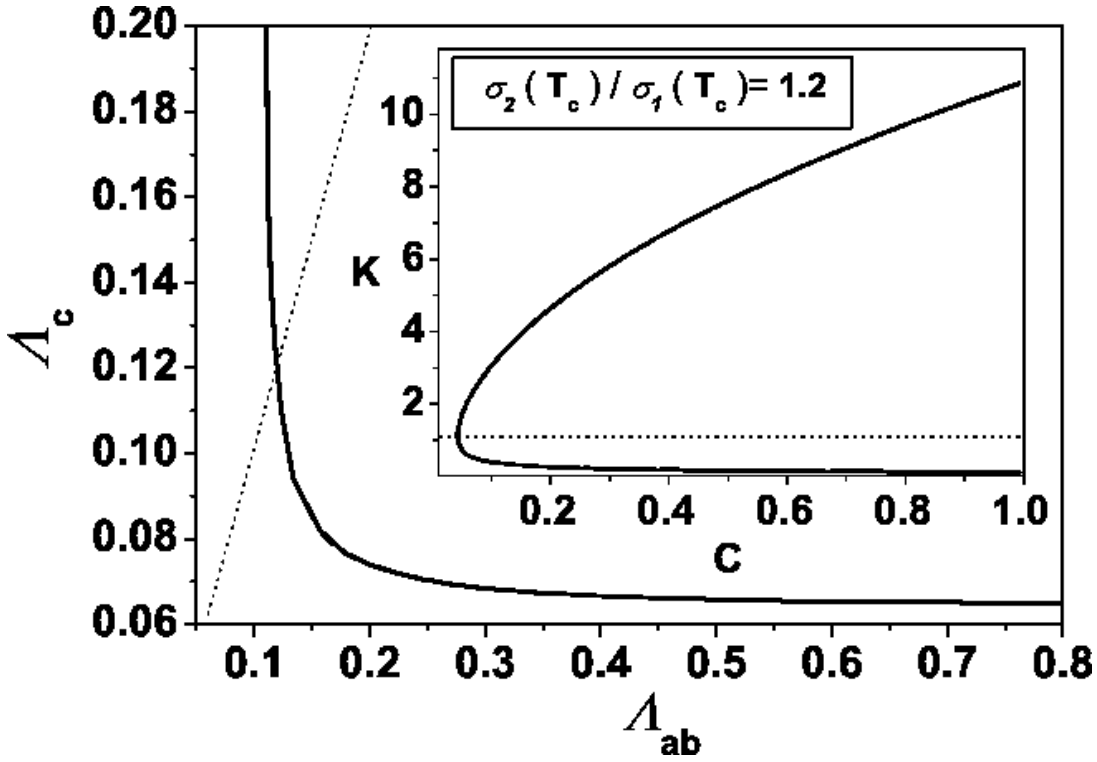
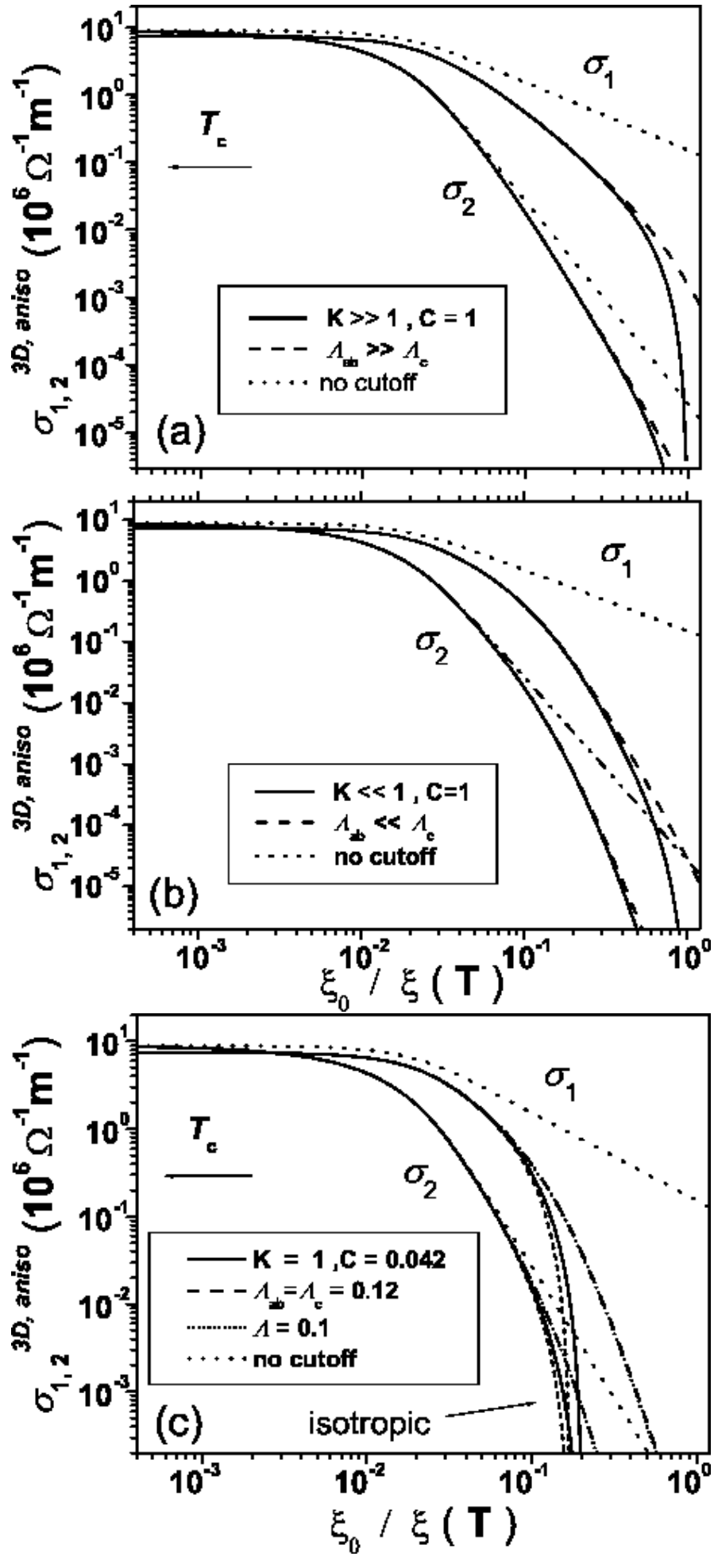


FIG. 2: Possible choices of the parameters Λ_{ab} and Λ_c when $(\sigma_2(T_c)/\sigma_1(T_c)) = 1.2$. The inset shows an alternative presentation in terms of the ratio $K = \Lambda_{ab}/\Lambda_c$ and the energy cutoff parameter C. The lower branch of this curve corresponds to the cases $\Lambda_{ab} \ll \Lambda_c$ while the upper branch is for $\Lambda_{ab} \gg \Lambda_c$. The crossover $\Lambda_{ab} = \Lambda_c$ is shown by the dotted line in the main panel, and $K = 1$ in the inset.


$\sigma_{1,2}^{3D,\,aniso}$ ($10^6 \Omega^{-1} m^{-1}$)
σ_1
σ_2
T_c
K >> 1 , C = 1
$\Lambda_{ab} >> \Lambda_c$
no cutoff
(a)
K << 1 , C=1
$\Lambda_{ab} << \Lambda_c$
no cutoff
(b)
K = 1 ,C = 0.042
$\Lambda_{ab}=\Lambda_c$ = 0.12
Λ = 0.1
no cutoff
isotropic
(c)
$\xi_0 / \xi(T)$

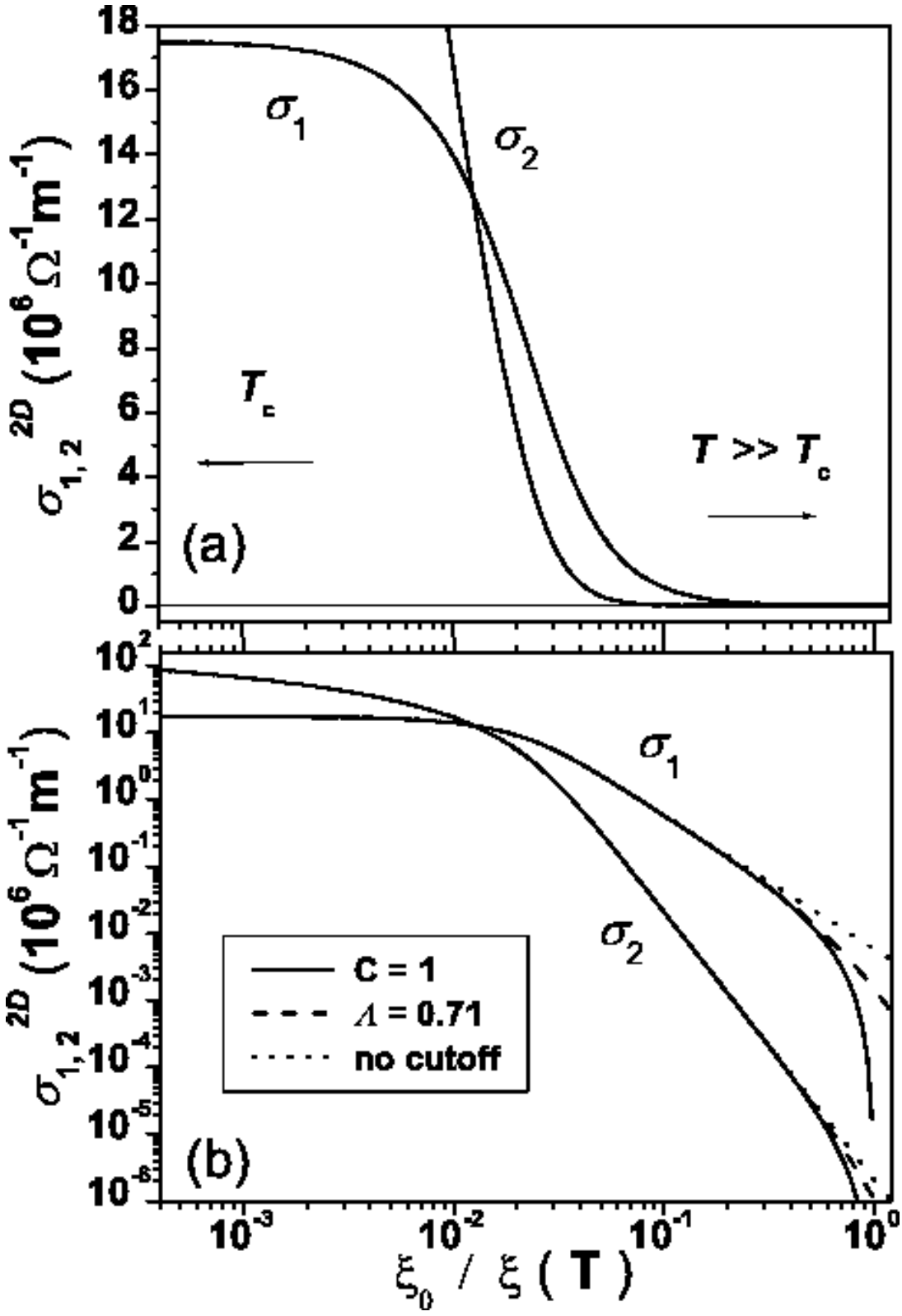


FIG. 4: Calculated *ac* fluctuation conductivities in the *2D* case. For the sake of comparison, the *2D* cutoff parameter ($\Lambda = 0.7$) is given the same value as Λ_{ab} of the *3D* case in Fig. 3(a). The style of the presentation follows that of Fig. 1.

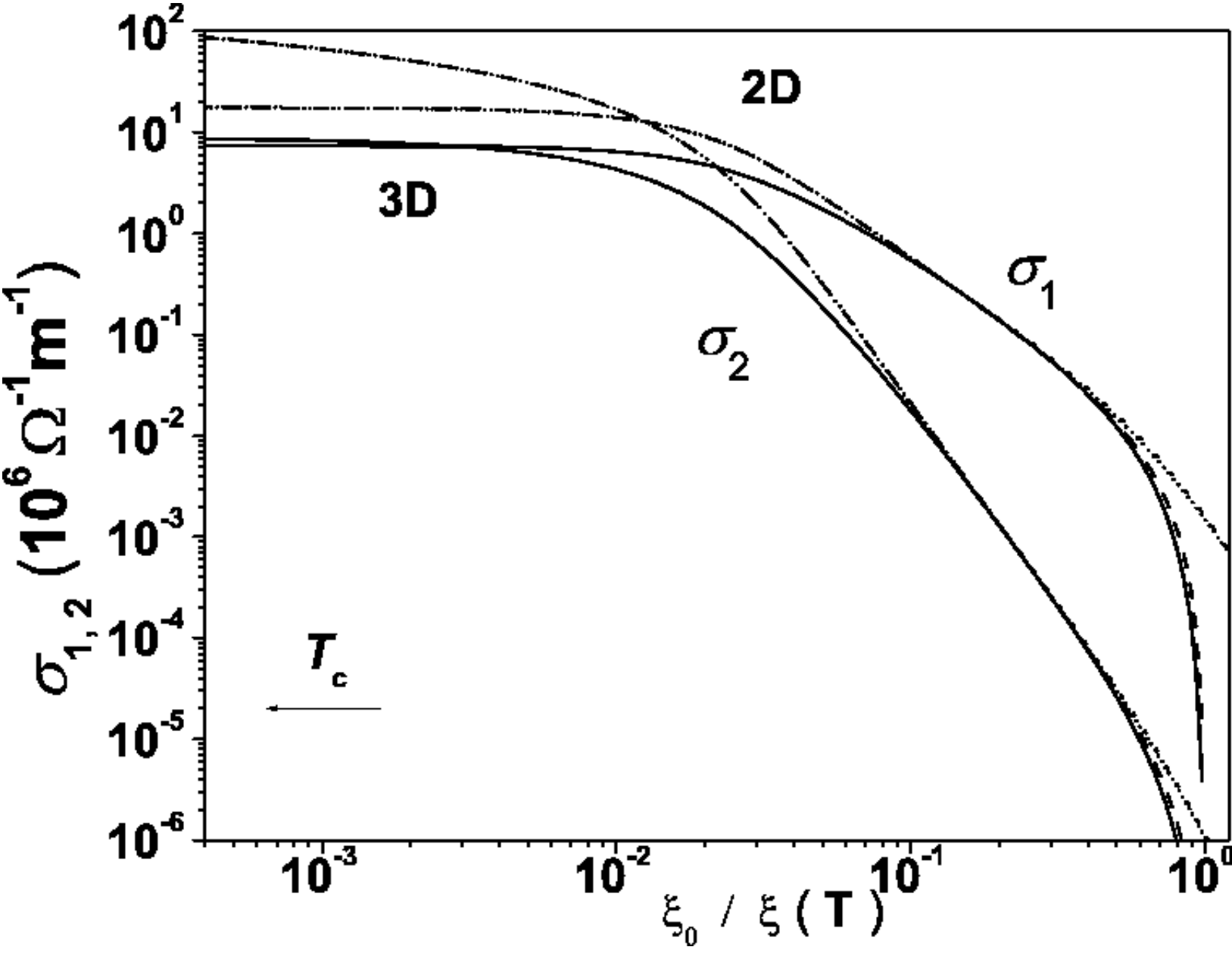


FIG. 5: Direct comparison of the *3D* and *2D* curves from Fig. 3(a) and Fig. 4, respectively, calculated with cutoff.

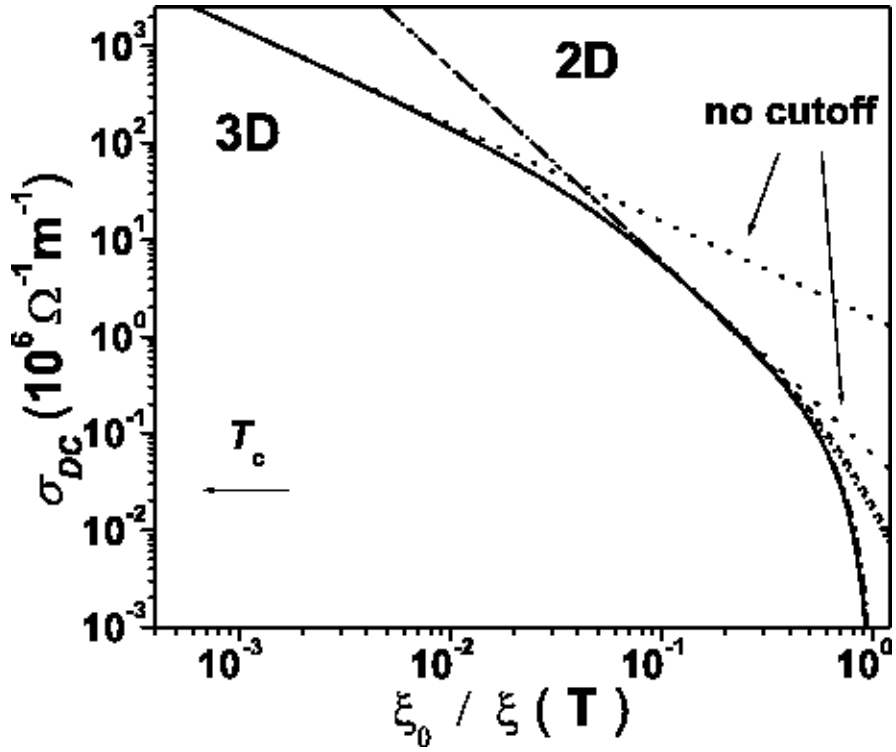


FIG. 6: Calculated *dc* fluctuation conductivities in the *3D* (full line), and *2D* (dashed line) cases with cutoff parameters as in Fig. 3(a) and Fig. 4, respectively. The calculations with no cutoff yield dotted lines with slopes $-1/2$, and -1 for the *3D* and *2D* cases, respectively.

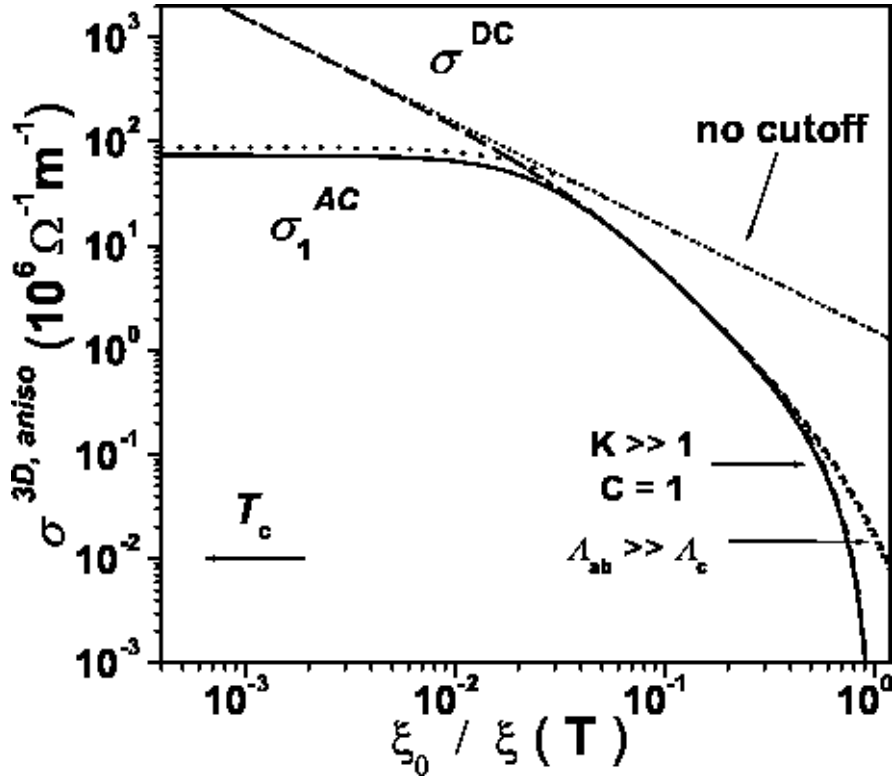


FIG. 7: Comparison of the *dc* fluctuation conductivity and the real part σ_1 of the *ac* case calculated with the same set of parameters in the *3D* expressions.

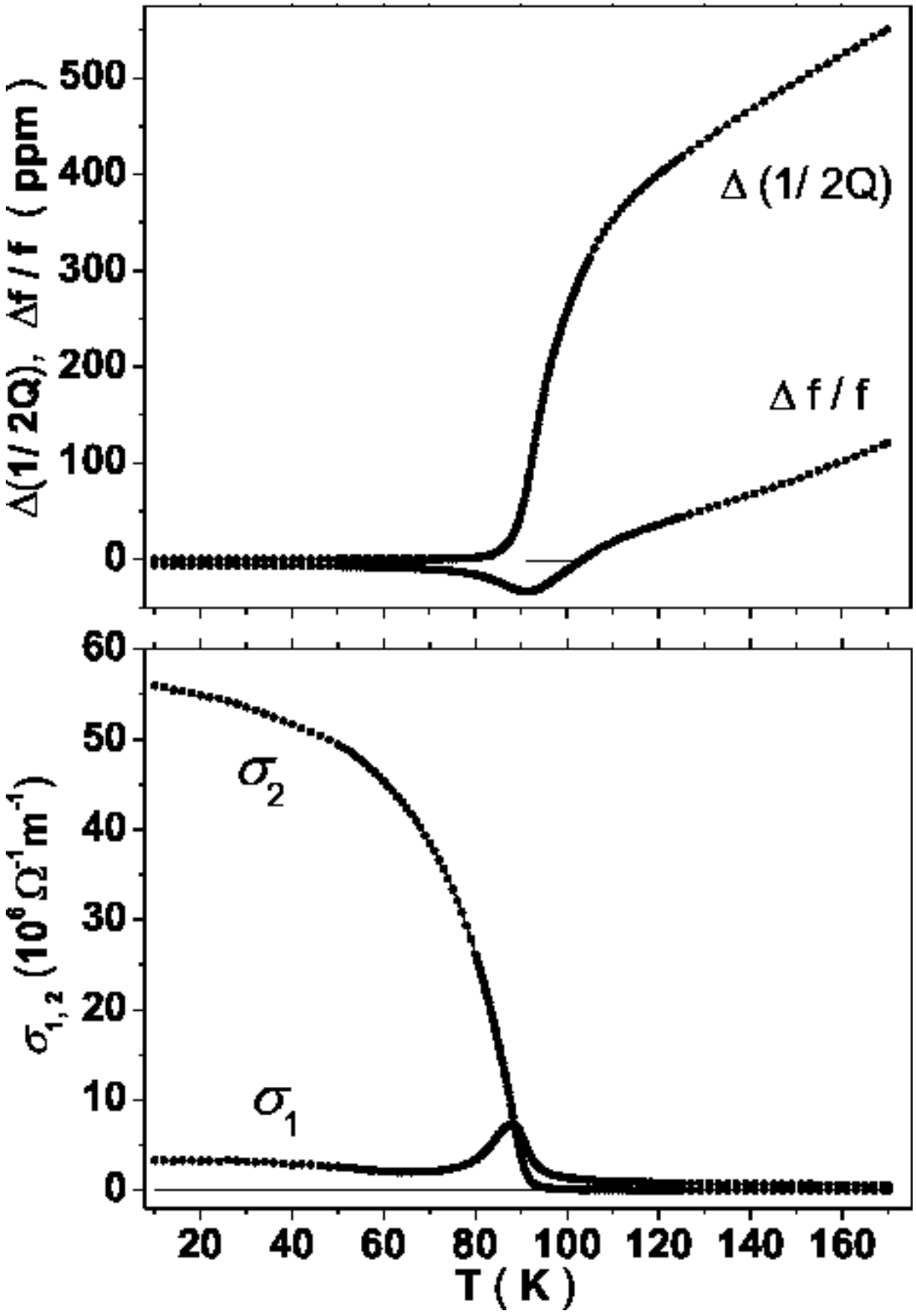


FIG. 8: Measured complex frequency shift in BSCCO-2212 thin film (a), and the deduced complex conductivity (b).

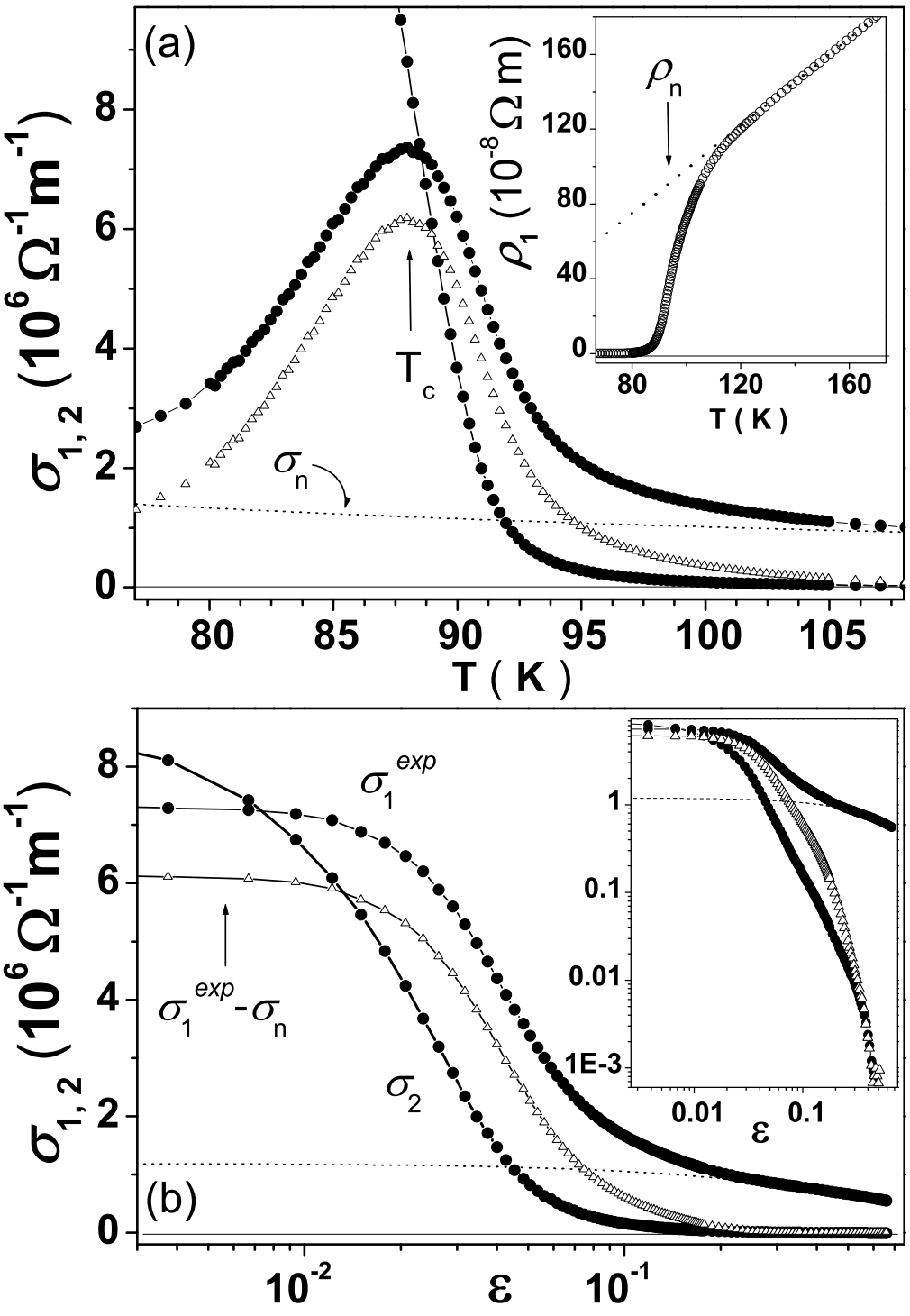


FIG. 9: (a) The real part of the fluctuation conductivity in BSCCO-2212 taken as either the total experimental value $\sigma_1 = \sigma_1^{exp}$ (•), or as the value obtained upon subtraction $\sigma_1 = \sigma_1^{exp} - \sigma_n$ (△), where σ_n is the normal conductivity obtained by extrapolation of the linear resistivity far above T_c (inset). The imaginary part σ_2 is background free and needs no subtraction. (b) Fluctuation conductivities above T_c as functions of the reduced temperature $\epsilon = \ln(T/T_c)$.

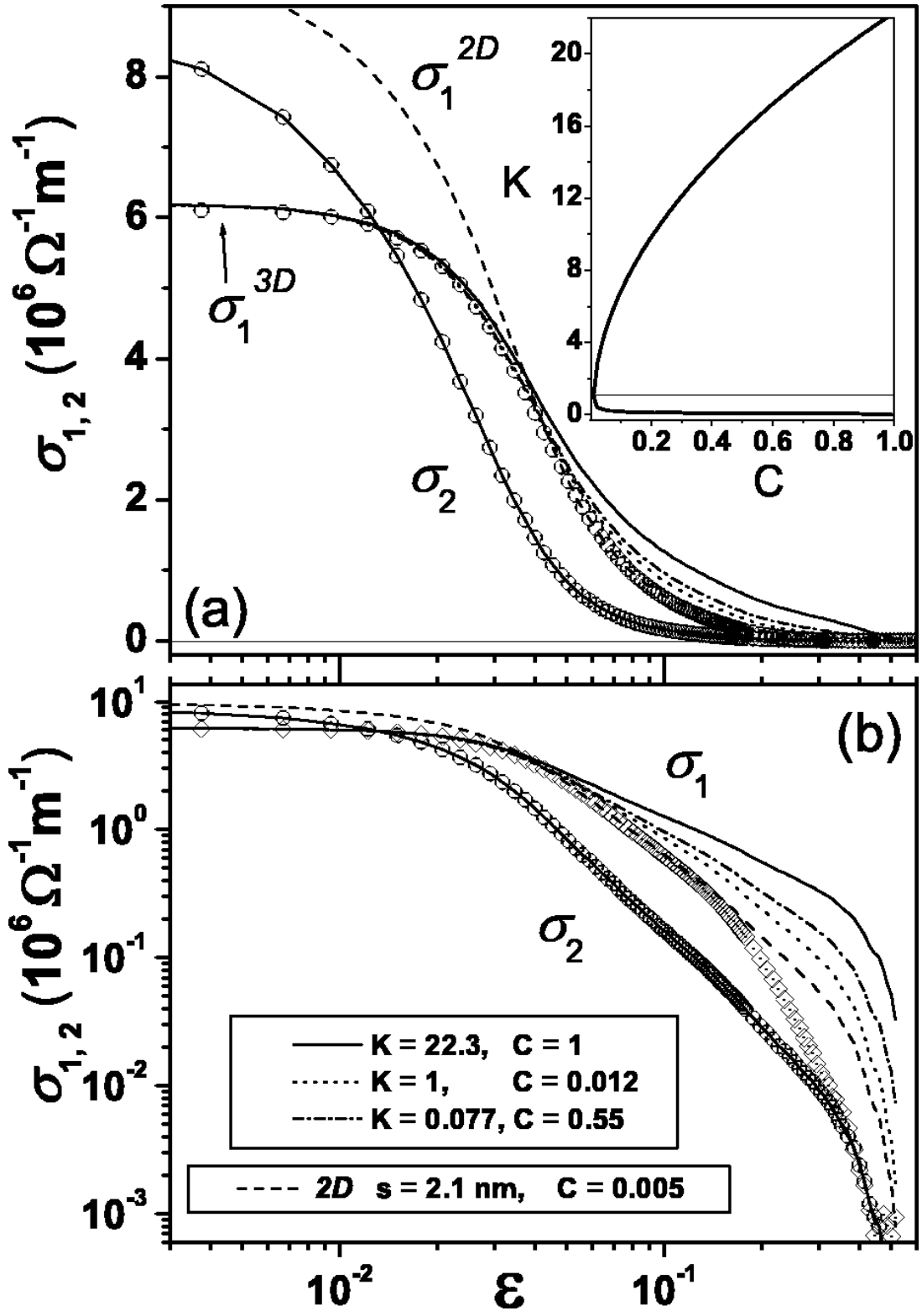


FIG. 10: The real part $\sigma_1 = \sigma_1^{exp} - \sigma_n$ and the imaginary part σ_2 of the fluctuation conductivity above T_c in BSCCO-2212. The inset shows the possible choices of the cutoff parameters for $\sigma_2/\sigma_1 = 1.46$ at T_c. The results of the calculations using the anisotropic *3D* and *2D* expressions are presented by the various curves in the main panel. The concomitant coherence lengths are given in Fig. 11.

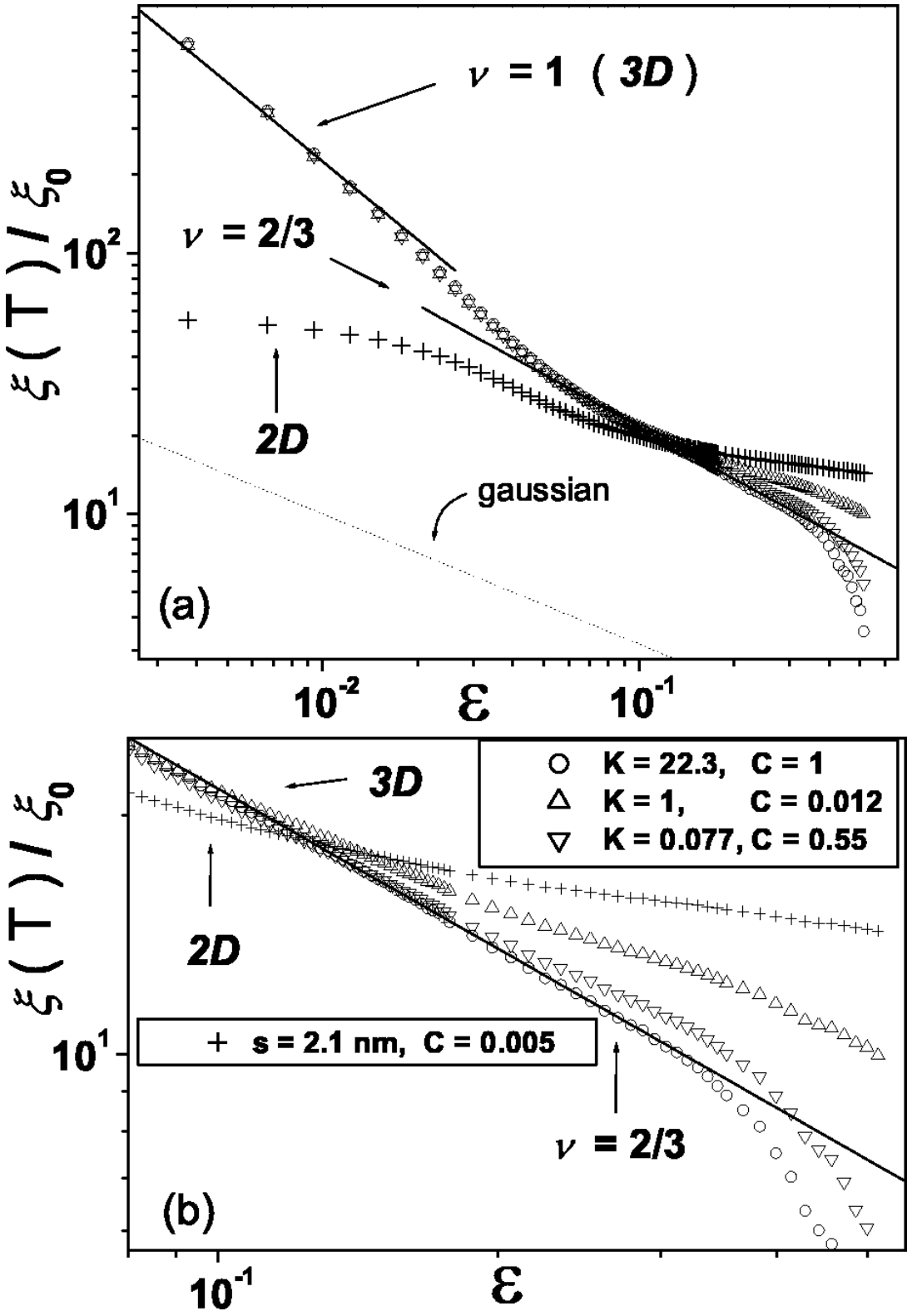


FIG. 11: The coherence lengths calculated from σ_2 using the various expressions and cutoff parameters as indicated in Fig. 10. The lower panel shows on an enlarged scale the slope 2/3 (full line) and the behavior of the various cases at higher temperatures.

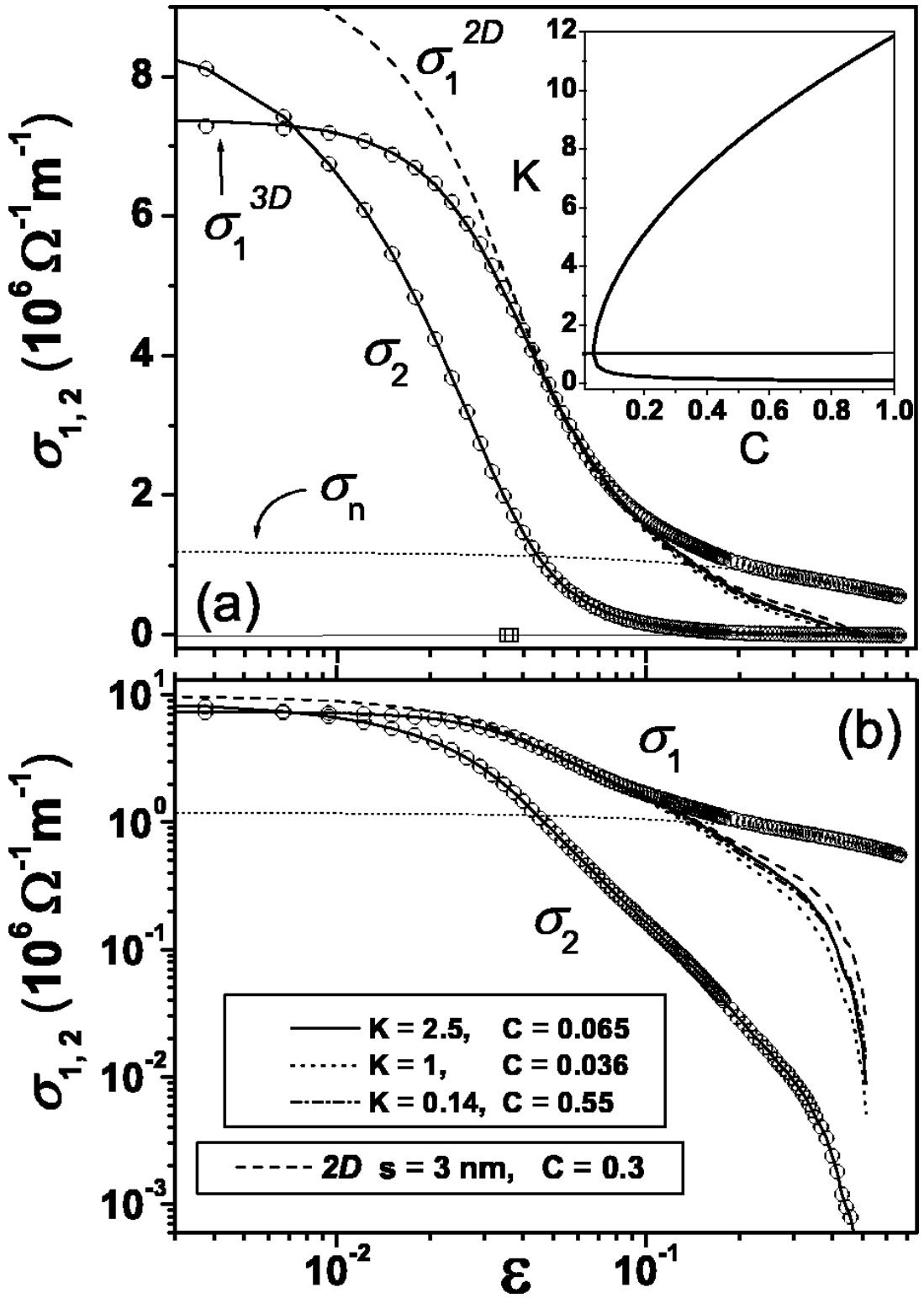


FIG. 12: The fluctuation conductivity in BSCCO-2212 taken as $\sigma_1 = \sigma_1^{exp}$ and σ_2 as measured. The inset shows the possible choices of the cutoff parameters for $\sigma_2/\sigma_1 = 1.22$ at T_c. The calculations were made for the *3D* and *2D* cases as indicated in the legend and described in the text. The concomitant coherence lengths are presented in Fig. 13.

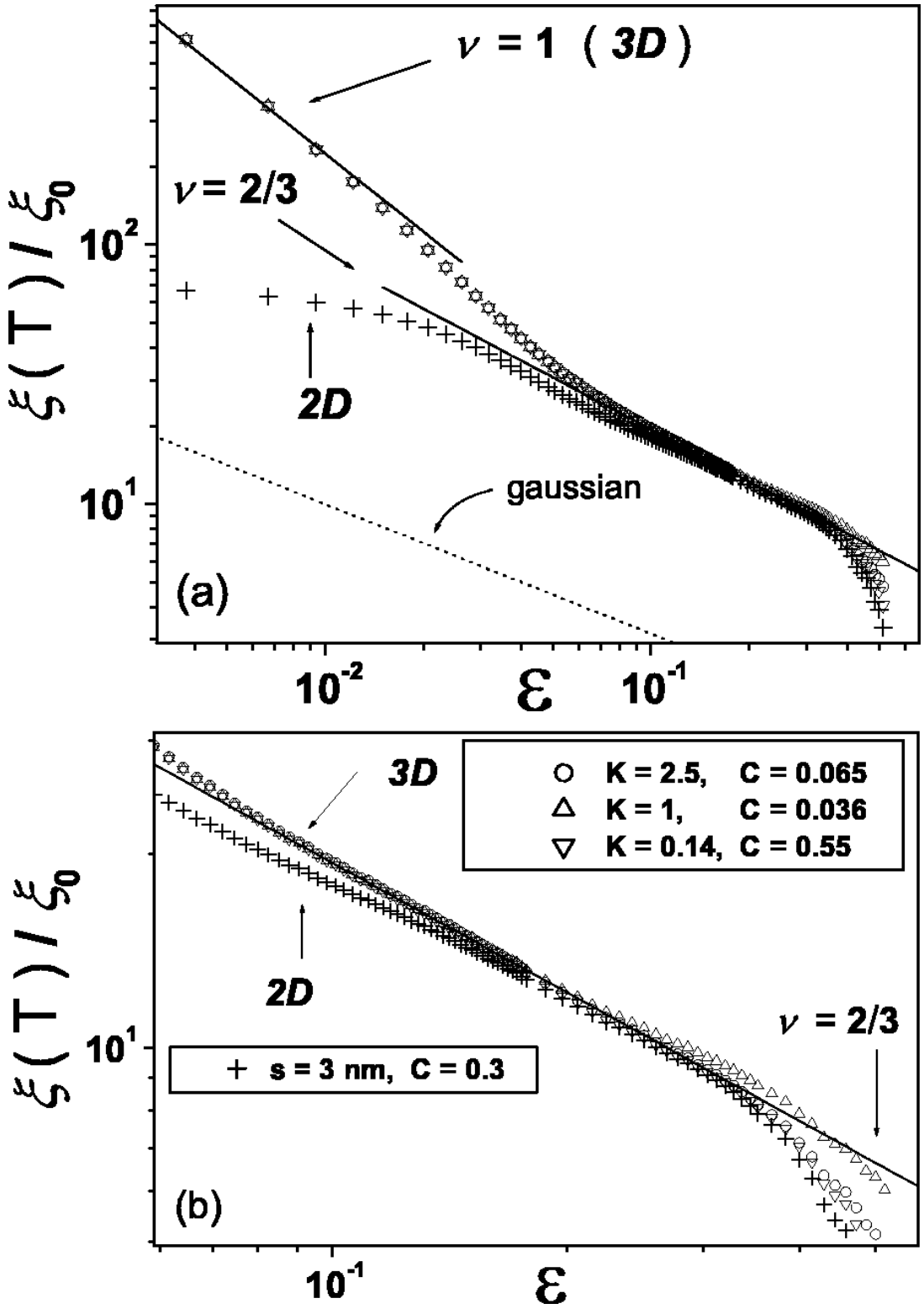


FIG. 13: The coherence lengths calculated from σ_2 in the various cases indicated in Fig. 12. The lower panel shows the high temperature behavior on an enlarged scale.

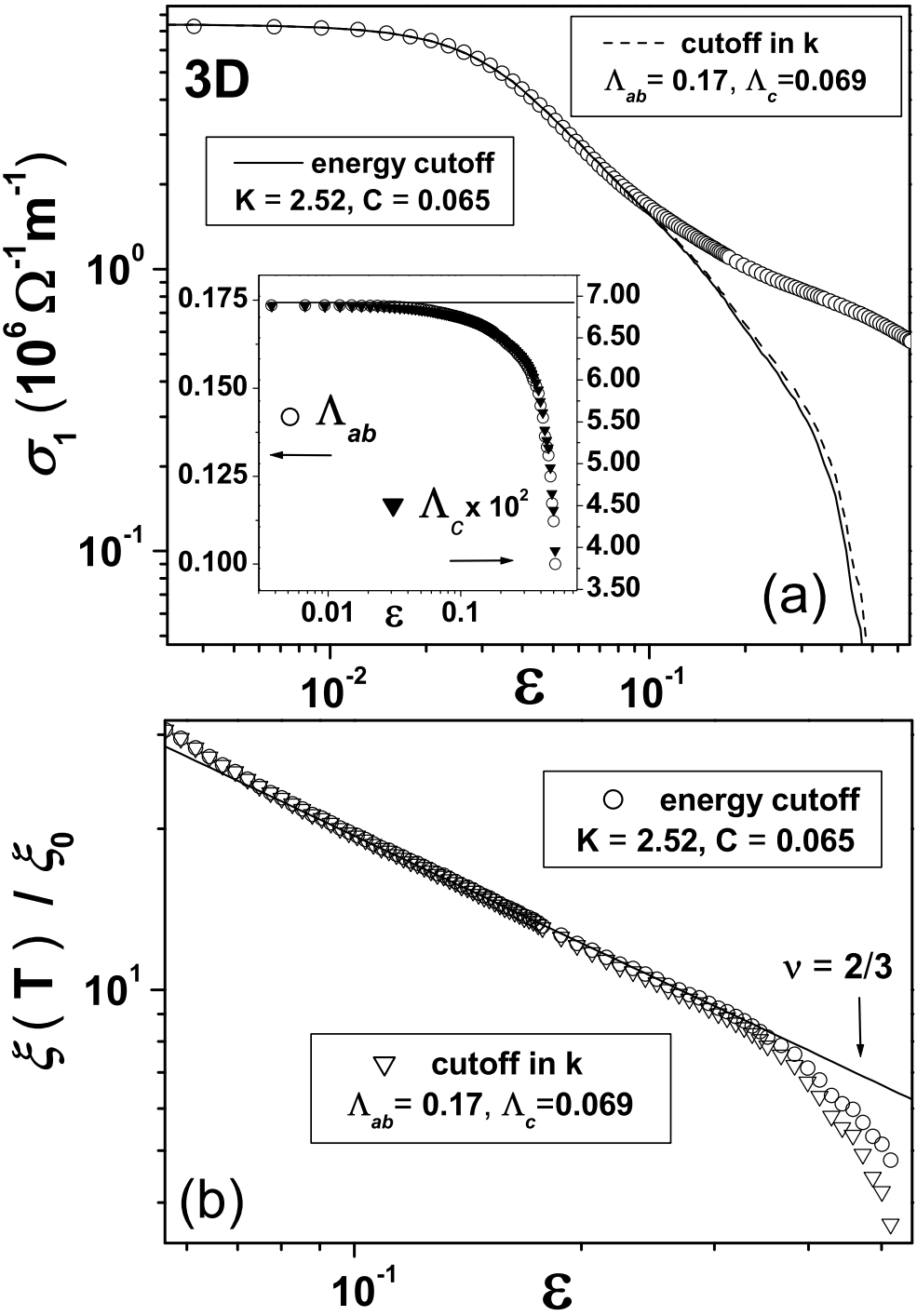


FIG. 14: Direct comparison of the calculations made with the wavevector cutoff and with the energy cutoff. In the former approach the Λ's are fixed at all temperatures while in the latter these parameters are reduced at higher temperatures as shown in the inset.

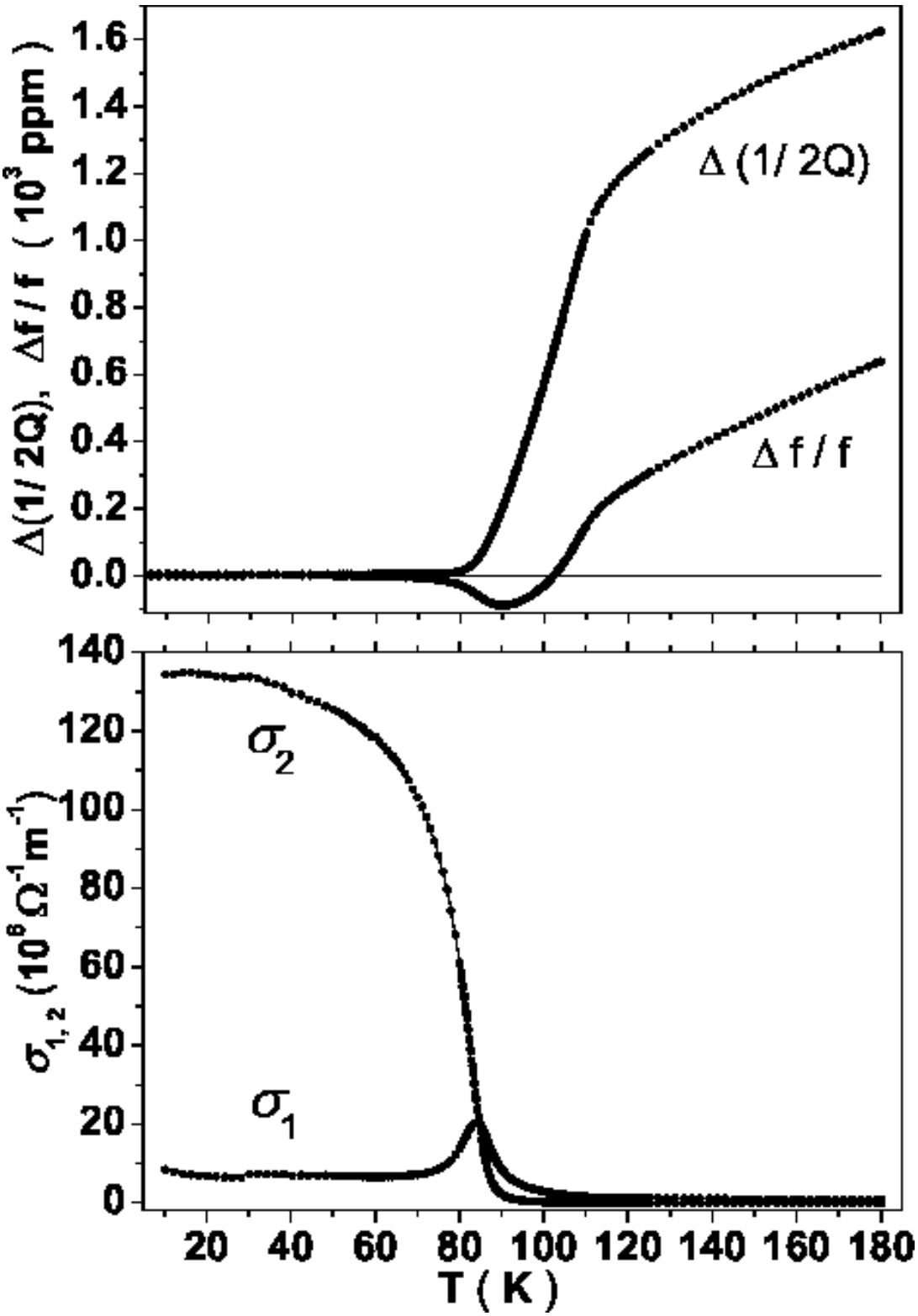


FIG. 15: Measured complex frequency shift and conductivity in BSCCO-2223 thin film.

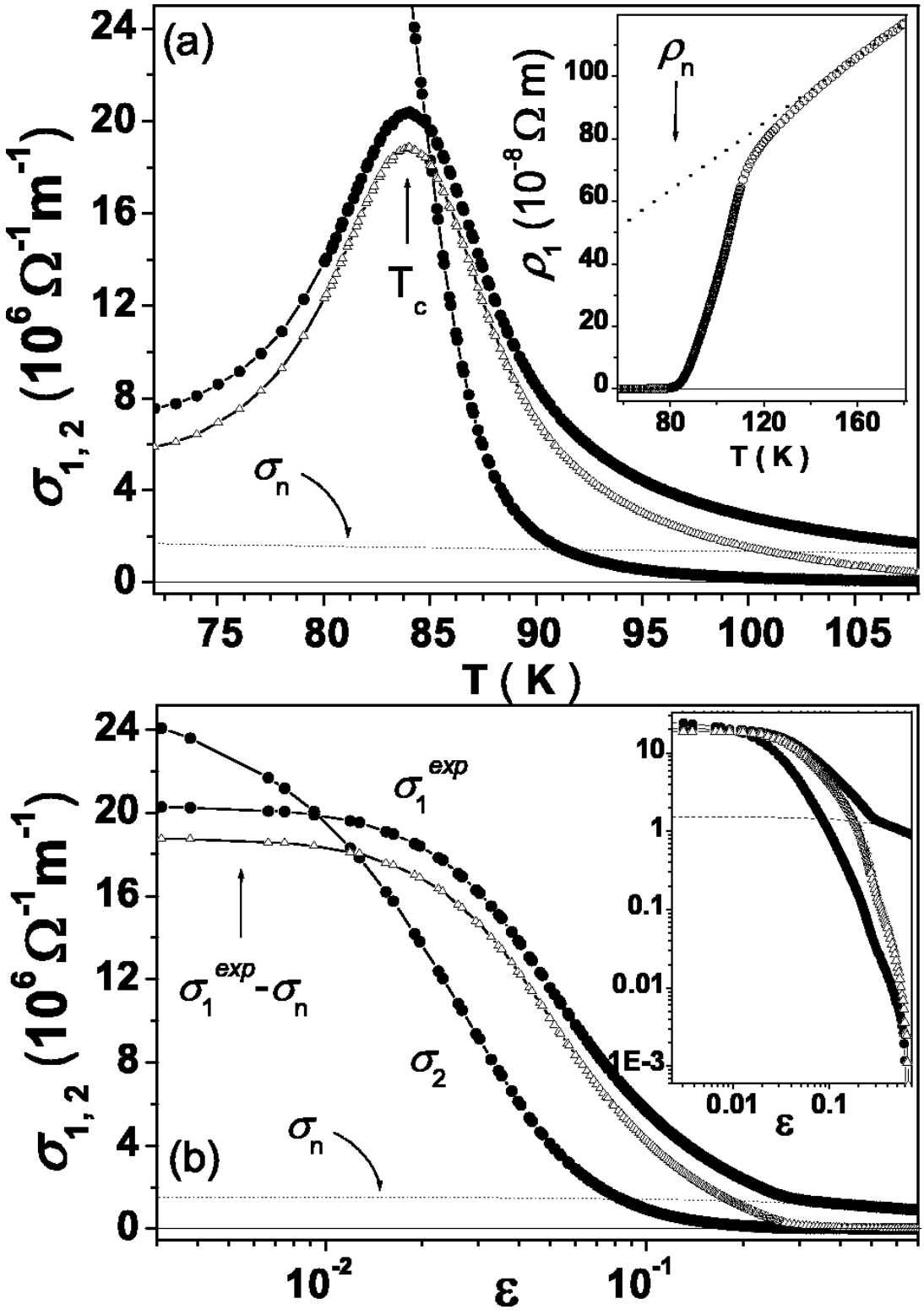


FIG. 16: (a) Complex conductivity in BSCCO-2223 near T_c. The extrapolated linear resistivity ρ_n is shown in the inset. The as measured σ_1^{exp} (•) and subtracted $\sigma_1^{exp} - \sigma_n$ (△) data sets are shown. (b) Fluctuation conductivities above T_c as functions of the reduced temperature $\epsilon = \ln(T/T_c)$.

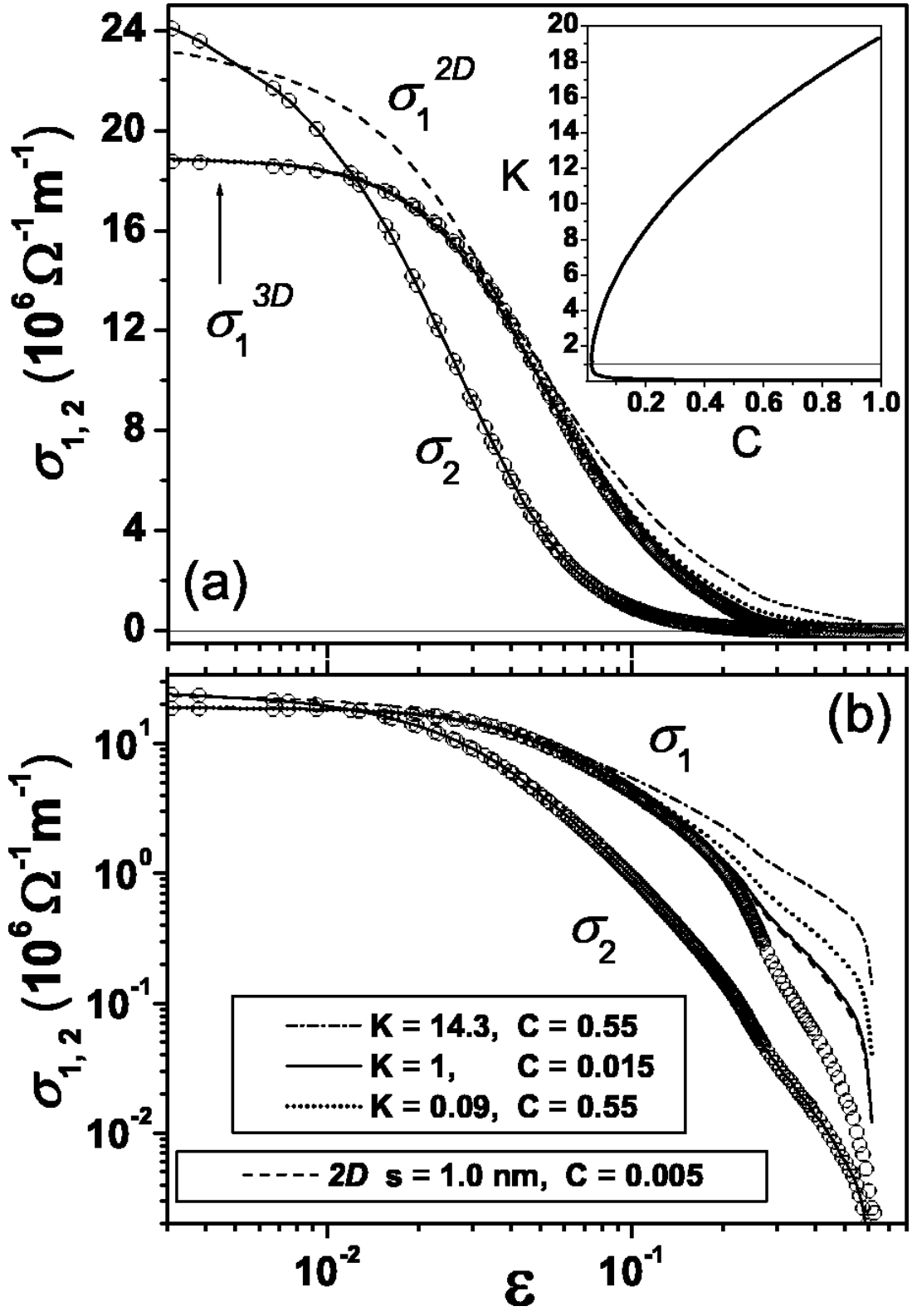


FIG. 17: Data analysis on the subtracted data set $\sigma_1^{exp} - \sigma_n$ and σ_2 in BSCCO-2223 thin film. The presentation is parallel to that of Fig. 10. The inset shows the possible choices of the cutoff parameters for $\sigma_2/\sigma_1 = 1.4$ at T_c.

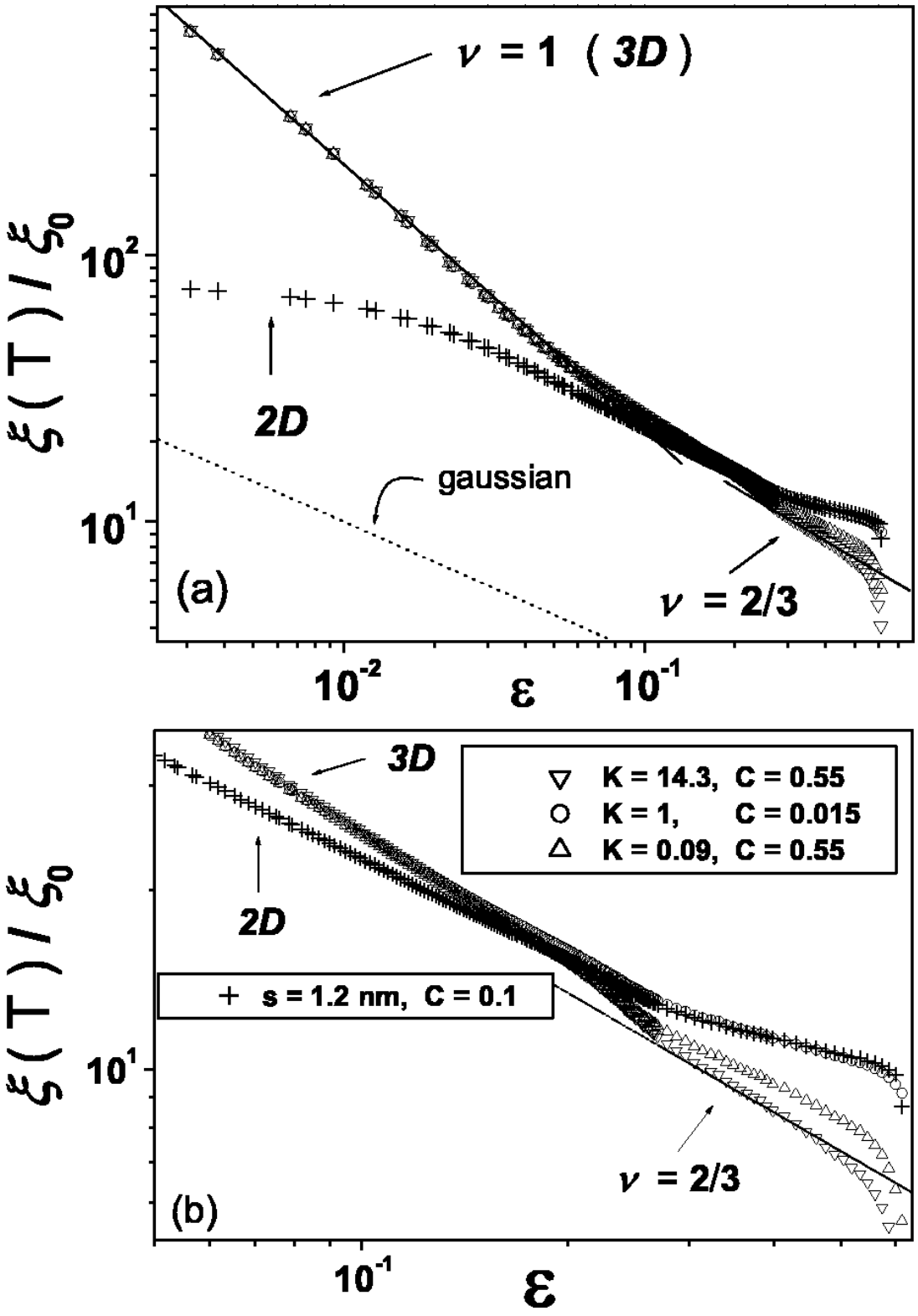


FIG. 18: The reduced coherence length calculated from σ_2 in the cases presented in Fig. 17.

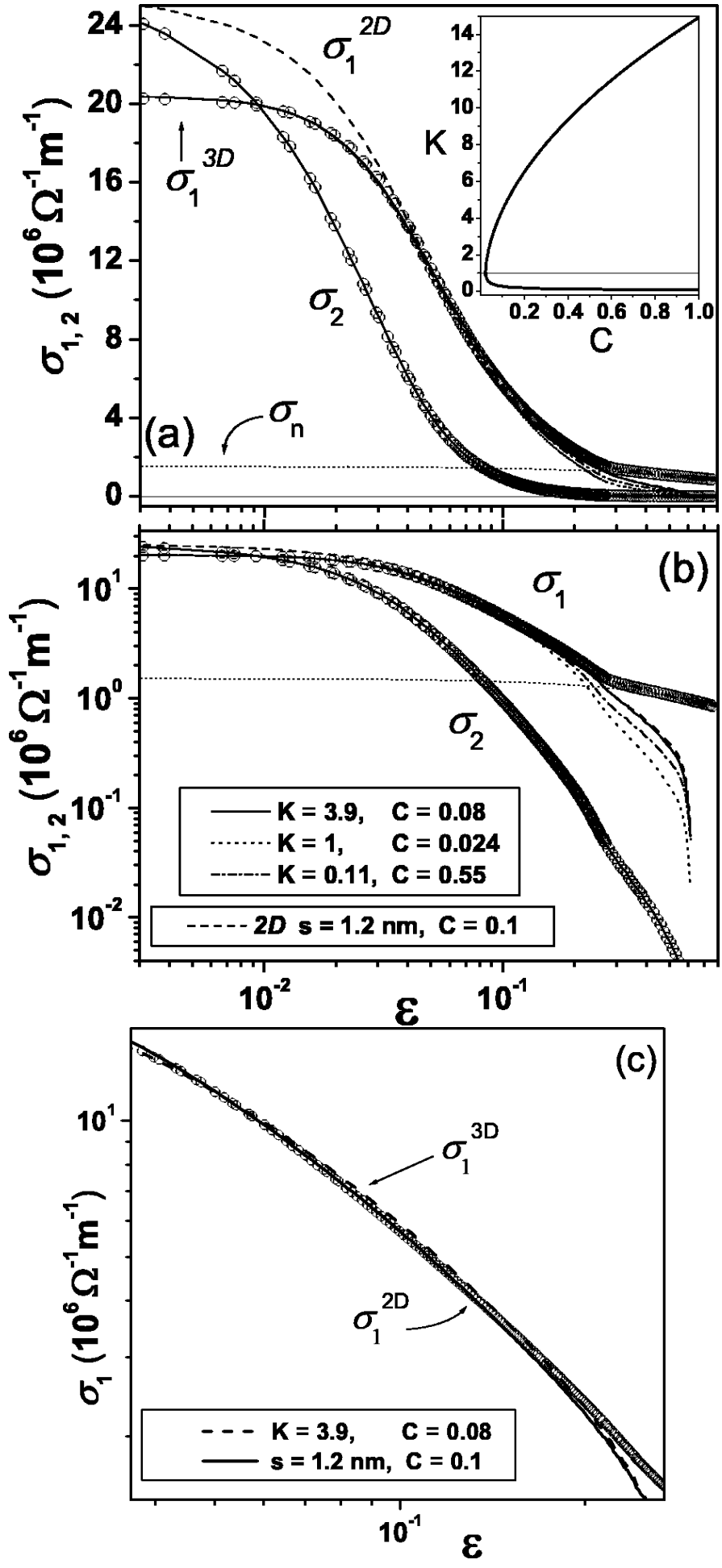


FIG. 10: The fluctuation conductivity in BSCCO-2223 taken as $\sigma_n = \sigma_n^{exp}$ and σ_n as measured. The inset shows the possible

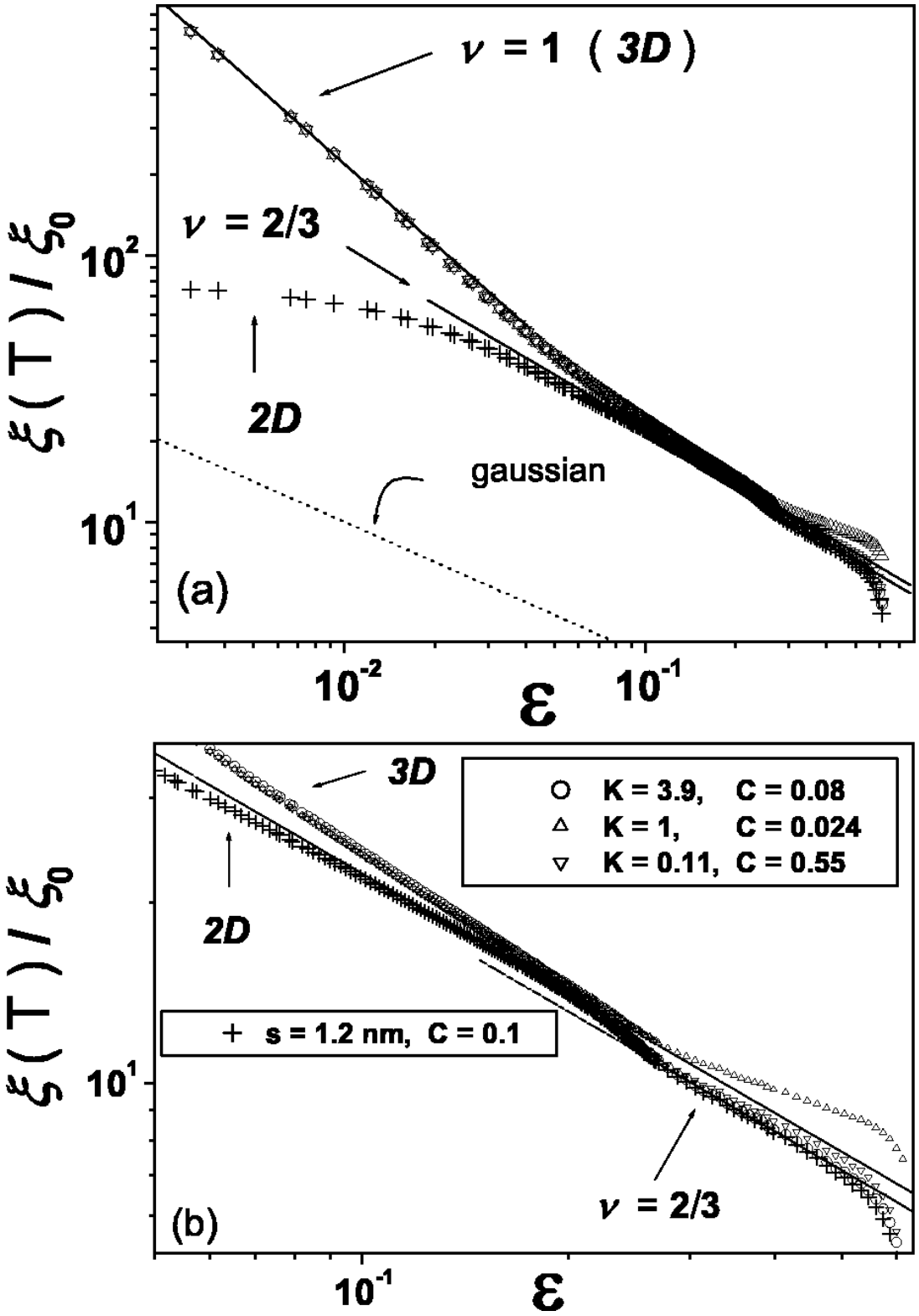


FIG. 20: The coherence lengths calculated from σ_2 in the various cases indicated in Fig. 19. The lower panel shows the high temperature behavior on an enlarged scale.

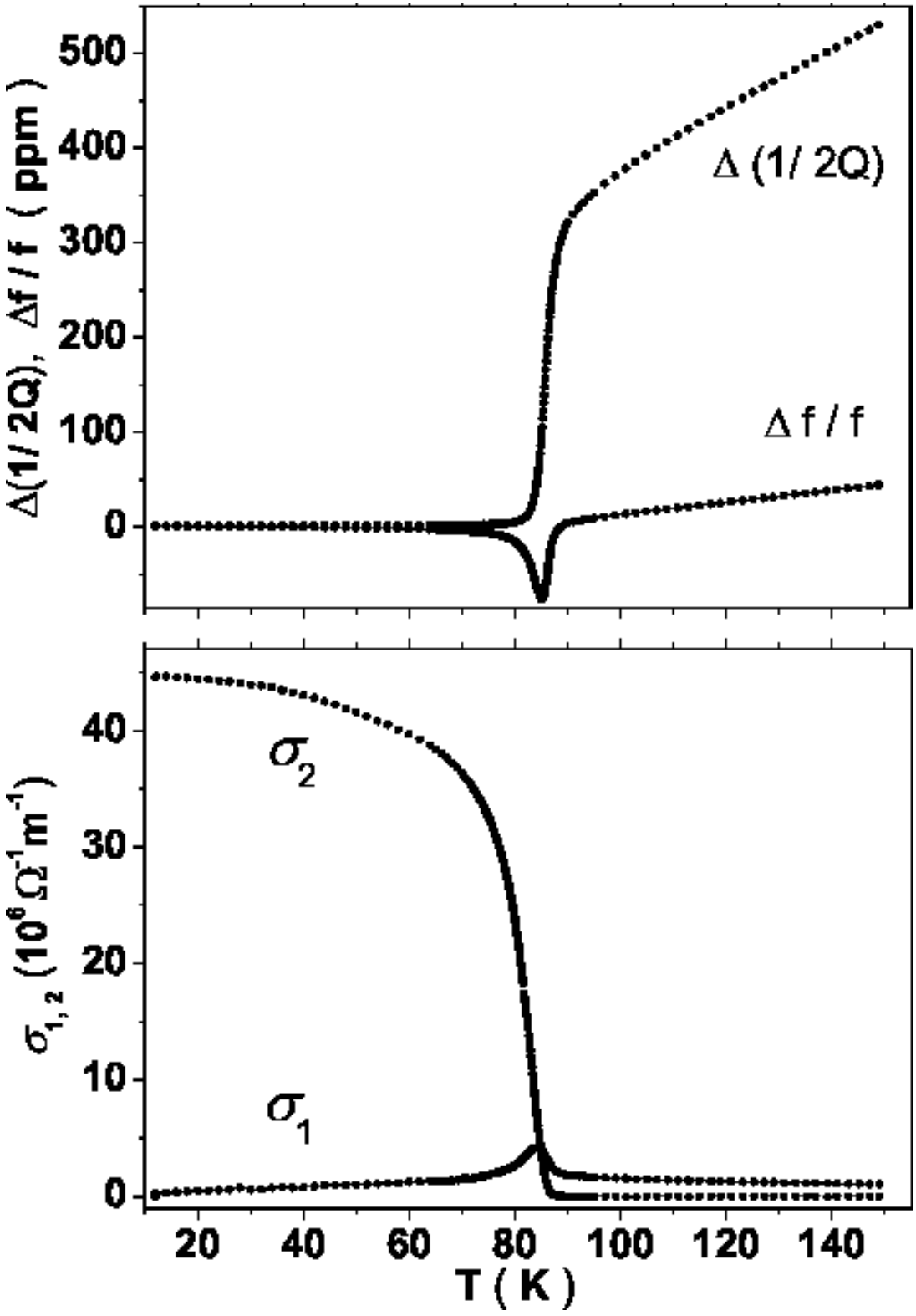


FIG. 21: Experimental complex frequency shift and conductivity in YBCO thin film

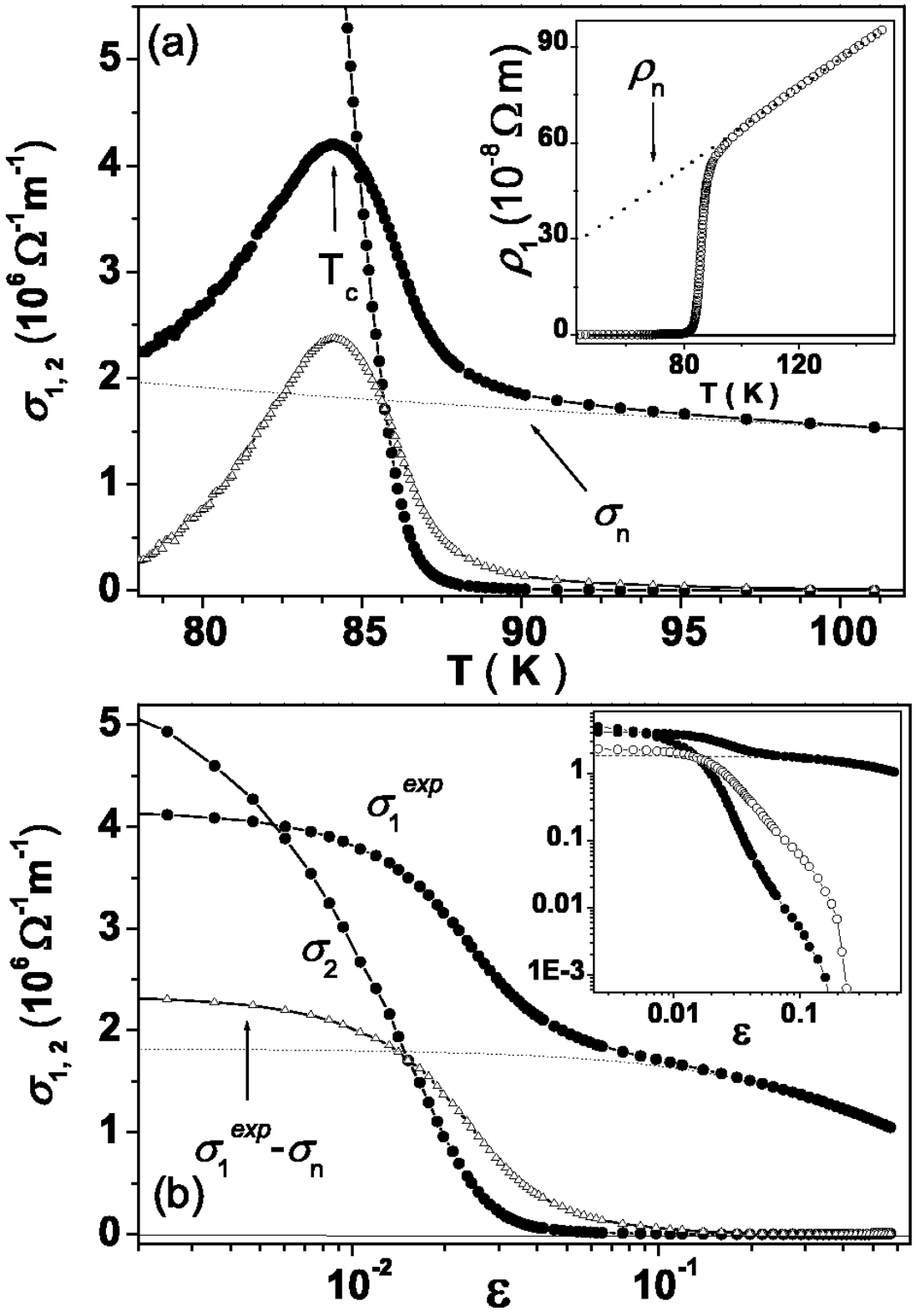


FIG. 22: (a) Complex conductivity in YBCO near T_c. The extrapolated linear resistivity ρ_n is shown in the inset. The as measured σ_1^{exp} (•) and subtracted $\sigma_1^{exp} - \sigma_n$ (△) data sets are shown. (b) Fluctuation conductivities above T_c as functions of the reduced temperature $\epsilon = \ln(T/T_c)$.

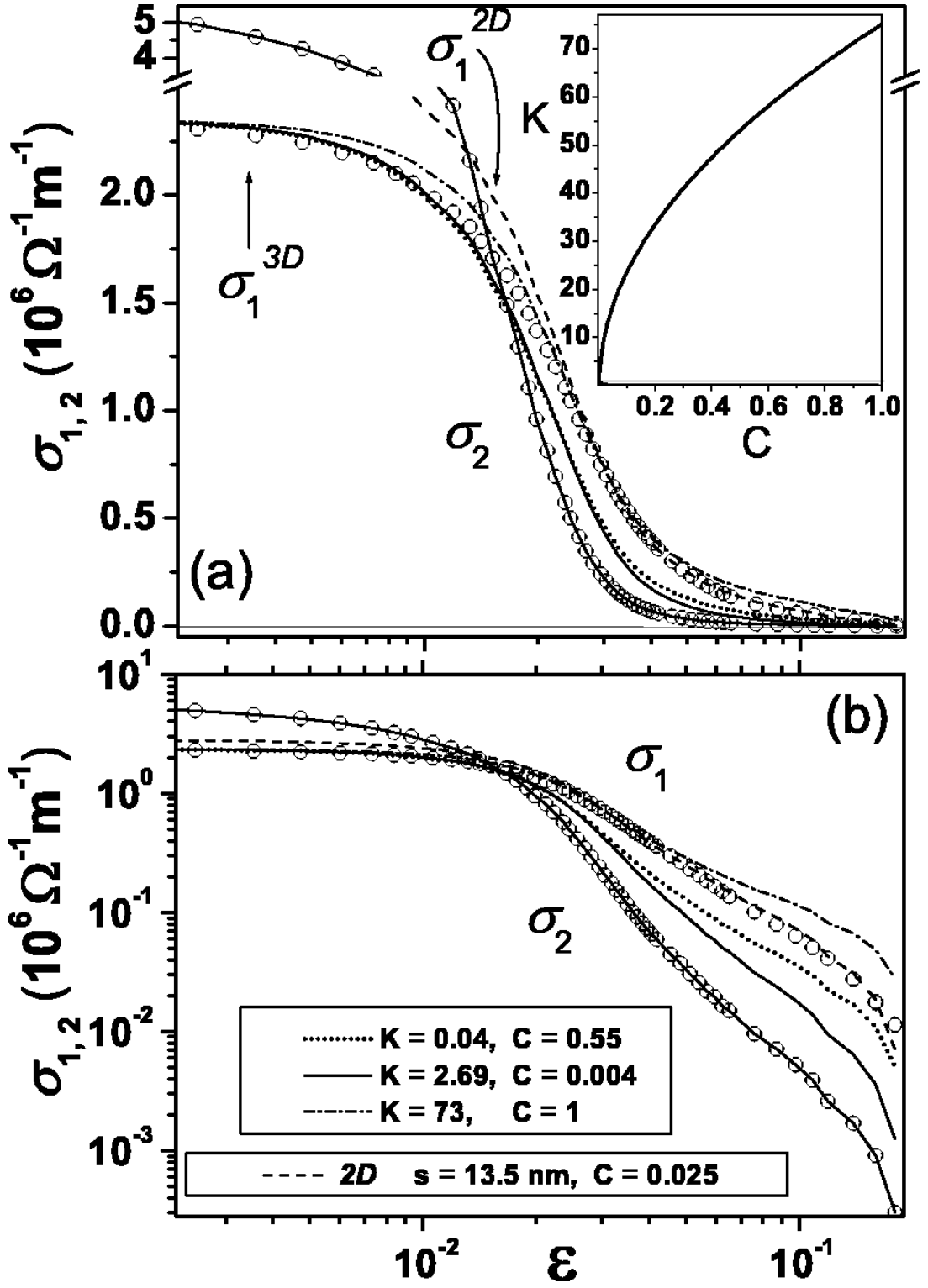


FIG. 23: Data analysis on the subtracted data set $\sigma_1^{exp} - \sigma_n$ and σ_2 in YBCO thin film. The presentation is parallel to that of Fig. 10. The inset shows the possible choices of the cutoff parameters for $\sigma_2/\sigma_1 = 2.42$ at T_c.

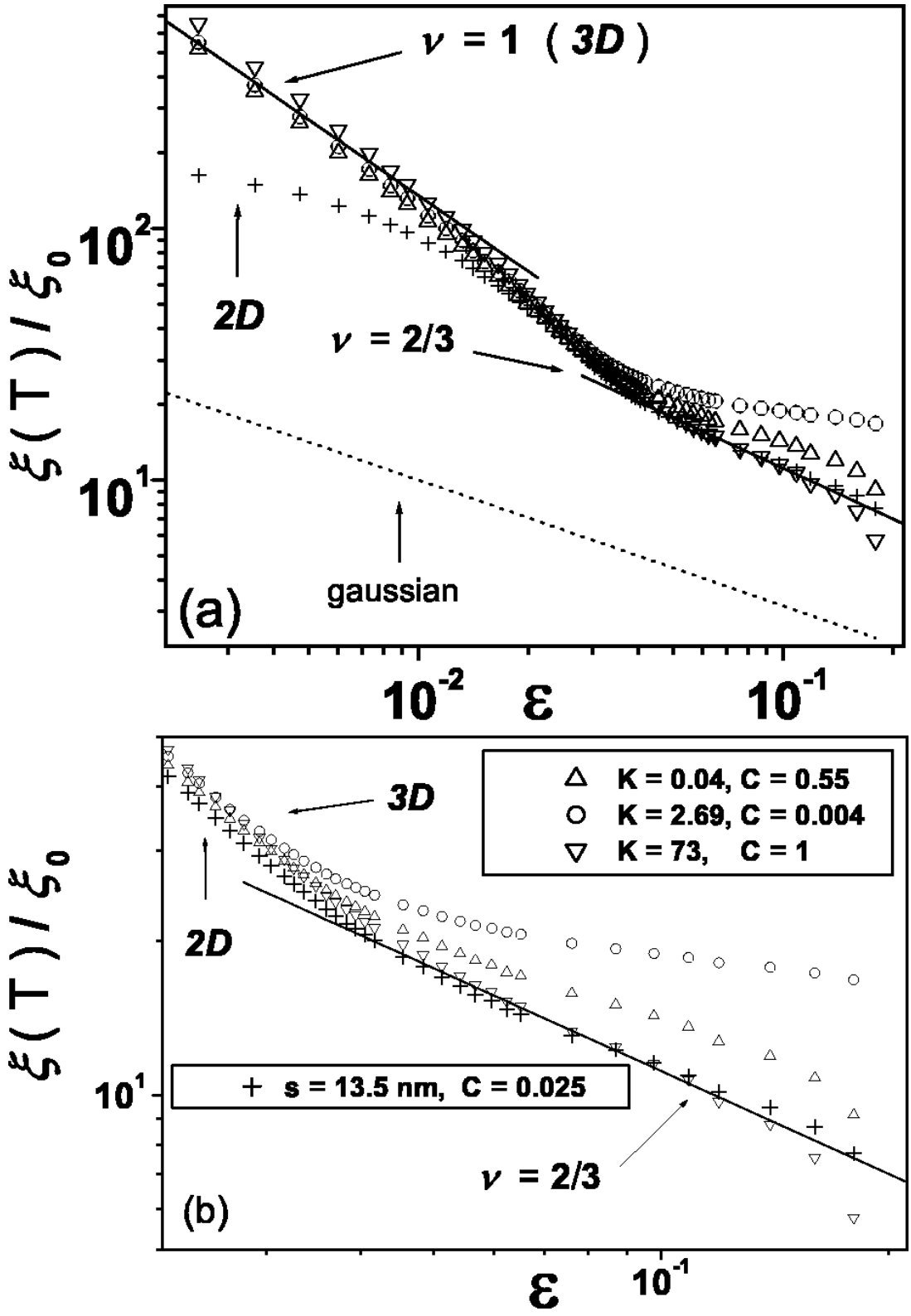


FIG. 24: The reduced coherence length calculated from σ_2 in the cases presented in Fig. 23.

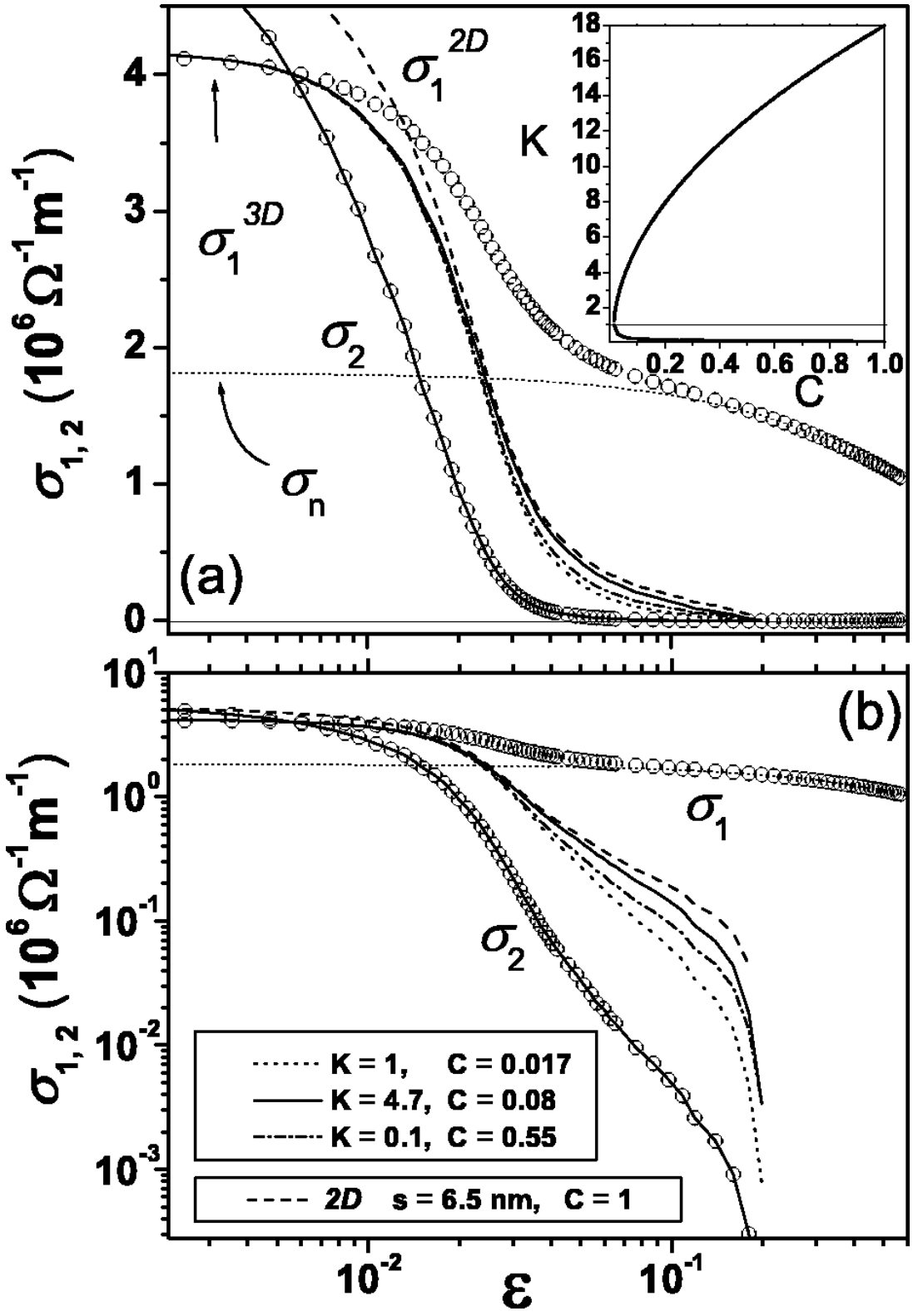


FIG. 25: The fluctuation conductivity in YBCO taken as $\sigma_1 = \sigma_1^{exp}$ and σ_2 as measured. The inset shows the possible choices of the cutoff parameters for $\sigma_2/\sigma_1 = 1.36$ at T_c. The calculations were made for the *3D* and *2D* cases as indicated in the legend and described in the text. The concomitant coherence lengths are presented in Fig. 26.

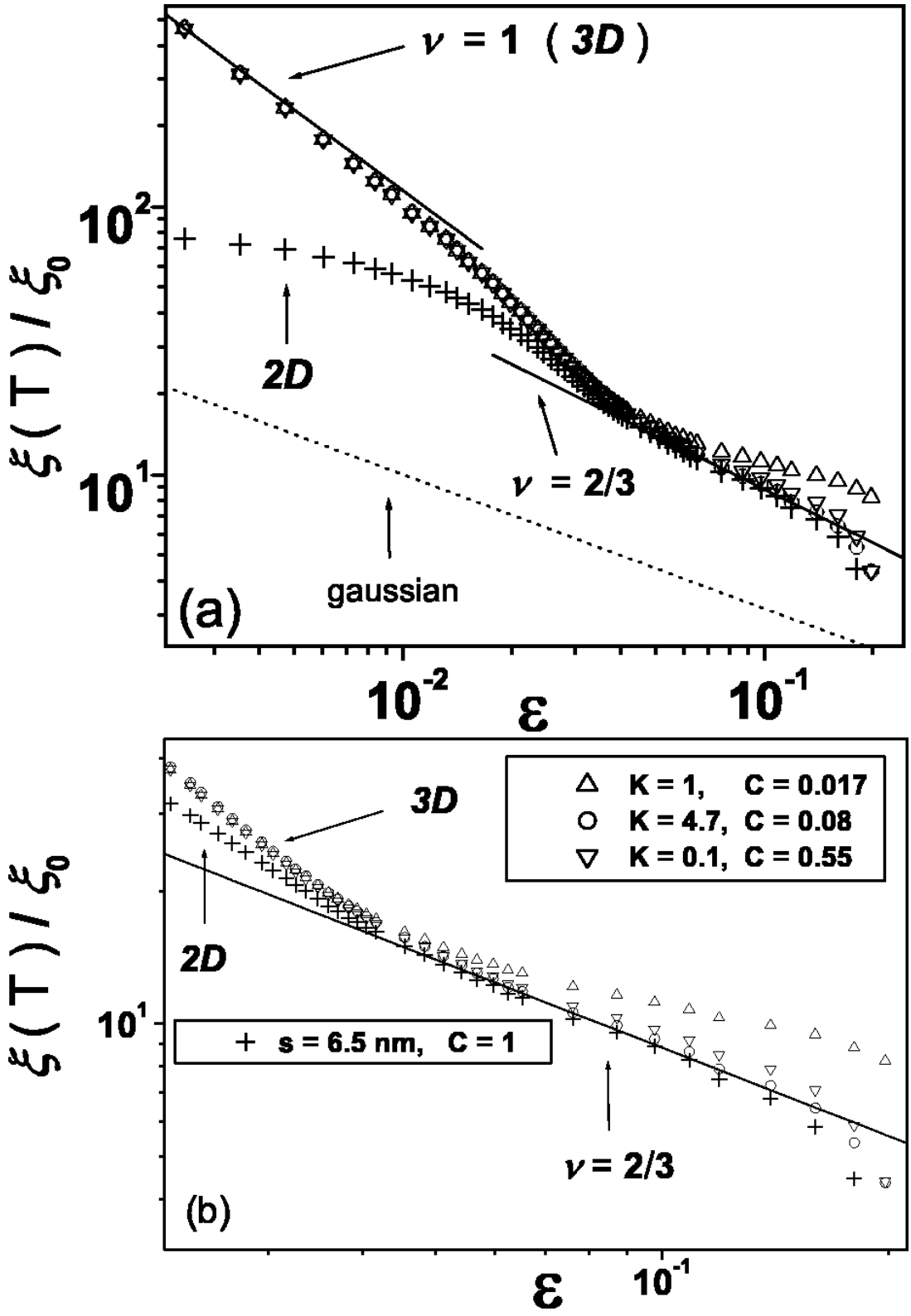


FIG. 26: The coherence lengths calculated from σ_2 in the various cases indicated in Fig. 25. The lower panel shows the high temperature behavior on an enlarged scale.

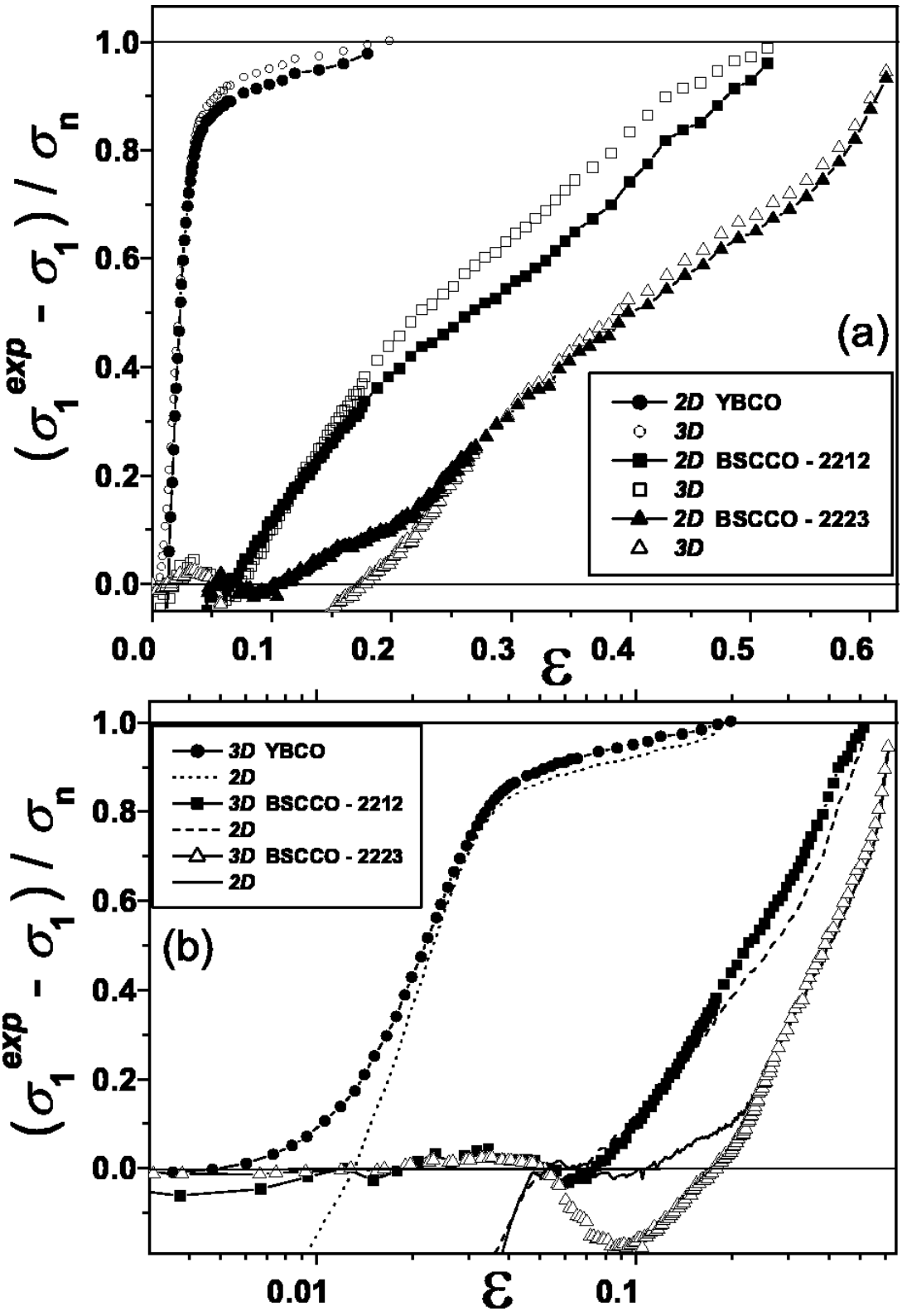


FIG. 27: The temperature dependence of the normal conductivity above T_c in our YBCO and BSCCO thin films. The values are given as fractions of the normal conductivity extrapolated from the behaviour at high enough temperatures where the resistivity is linear.